

Die approbierte Originalversion dieser Diplom-/Masterarbeit ist an der Hauptbibliothek der Technischen Universität Wien aufgestellt (<http://www.ub.tuwien.ac.at>).

The approved original version of this diploma or master thesis is available at the main library of the Vienna University of Technology (<http://www.ub.tuwien.ac.at/englweb/>).

Unterschrift des Betreuers



TECHNISCHE
UNIVERSITÄT
WIEN
Vienna University of Technology

DIPLOMARBEIT

Investigation of SrTiO₃(001) and (110) Surfaces

Ausgeführt am Institut für Angewandte Physik
der Technischen Universität Wien

unter der Anleitung von Prof. Dr. Ulrike Diebold
und PhD Zhiming Wang

durch

Stefan Gerhold

Grundsteingasse 22/207 1160 Wien

Datum

Unterschrift (Student)

Abstract

Strontium titanate (SrTiO_3) belongs to the class of cubic perovskite-type oxides and it is well known because of several interesting effects taking place in its bulk and on its surfaces. Effects are ranging from superconductivity, to photo electrolysis, and to the formation of a two dimensional electron gas at its surfaces and interfaces.

We studied the creation and the characteristics of surface reconstructions on the $\text{SrTiO}_3(110)$ and (001) surfaces using STM, LEED, XPS and ISS. We also performed XAS and high resolution photoemission spectroscopy (XPS, UPS) measurements on the $\text{SrTiO}_3(110)$ surface using synchrotron radiation in MAXLab, Lund. Atomically well-defined SrTiO_3 surfaces were obtained by Ar^+ sputtering and annealing.

The commonly observed $\text{SrTiO}_3(110)$ (4×1) reconstruction consists of a layer of TiO_4 tetrahedra. XAS results confirm a tetrahedral coordination for titanium atoms in the surface layers of the (4×1) reconstruction. UPS spectra show the valence band and the band gap with no in-gap state. However, prolonged exposure to synchrotron light produces an in-gap state, which comes from oxygen vacancies.

Wang et al. [Phys. Rev. B, 83, 155453 (2011)] reported a surface phase diagram of $\text{SrTiO}_3(110)$ that clearly shows that with increasing titanium evaporation dosage, the surface transforms from a series of $(n\times 1)$ ($n = 6, 5, 4$) to $(m\times 4)$ ($m = 2, 6$) and, finally, to $(1\times l)$ ($l = 4, 5$) reconstructions. Reversible transitions are obtained by increasing the strontium evaporation dosage. This thesis reports that also on the $\text{SrTiO}_3(001)$ surface, structures can be changed reversibly in a similar manner.

For the $\text{SrTiO}_3(001)$ surface numerous reconstructions are reported in the literature. We studied the $c(4\times 2)$ and (2×2) surface reconstructions and a (1×1) terminated surface. Reconstructions on the $\text{SrTiO}_3(001)$ surface are believed to either consist of oxygen vacancies, strontium adatoms, or a double layer TiO_2 structure. We are able to reversibly switch between the reconstructions by evaporating strontium or titanium followed by annealing. Models proposed in the literature for the $c(4\times 2)$ and the (2×2) reconstructions show an identical surface stoichiometry, which is in contrast to the results presented here.

This work was supported in part by the ERC Advanced Grant 'Oxide Surfaces'.

Zusammenfassung

Strontiumtitanat (SrTiO_3) zählt zu den Oxiden mit kubischer Perowskit-Struktur und ist für interessante Effekte bekannt, welche sich sowohl im Festkörper als auch auf der Oberfläche zeigen. Zu diesen Effekten zählen unter anderem die Supraleitung, die Photolyse sowie die Existenz von zweidimensionalen Elektronengasen.

In dieser Arbeit wurden mit Hilfe von STM, LEED, XPS und ISS die Erzeugung und die Eigenschaften einiger Rekonstruktionen auf den $\text{SrTiO}_3(110)$ und (001) Oberflächen untersucht. Weiters wurden XAS und hochaufgelöste Photoemissionsspektroskopie (XPS, UPS) unter Verwendung von Synchrotronstrahlung am MAXLab in Lund durchgeführt. Die Erzeugung von atomar geordneten SrTiO_3 Oberflächen erfolgte durch Argon-Ionen Zerstäubung und Ausheilen in Sauerstoff.

Das Strukturmodell der $\text{SrTiO}_3(110)$ (4×1) Rekonstruktion enthält an der Oberfläche eine Schicht von TiO_4 Tetraedern. Die XAS Ergebnisse bestätigen die tetraedrische Koordination der Titanatome in der Oberflächenschicht der (4×1) Rekonstruktion. UPS-Spektren zeigen, dass durch eine längere Einwirkung von Synchrotronstrahlung ein elektronischer Zustand innerhalb der Bandlücke erzeugt werden kann. Dieser konnte auf Sauerstoff-Fehlstellen zurückgeführt werden.

Wang et al. [Phys. Rev. B, 83, 155453 (2011)] entwickelten ein Oberflächen-Phasendiagramm, welches veranschaulicht, dass sich die $\text{SrTiO}_3(110)$ Oberfläche mit zunehmendem Aufdampfen von Titan von einer Reihe mit $(n\times 1)$ ($n = 6, 5, 4$) zu $(m\times 4)$ ($m = 2, 6$) und schlussendlich zu $(1\times l)$ ($l = 4, 5$) überführen lässt. Diese Reihenfolge kann durch Aufdampfen von Strontium umgekehrt werden. Die vorliegende Arbeit zeigt, dass sich Strukturen ebenso auf der (001) Oberfläche von SrTiO_3 reversibel ineinander überführen lassen.

Die $\text{SrTiO}_3(001)$ Oberfläche wurde bereits ausgiebig erforscht. Dass auf dieser Oberfläche eine Vielzahl an Rekonstruktionen existiert, wird vor allem im Literaturüberblick ersichtlich. Die vorliegende Arbeit befasste sich sowohl mit der $c(4\times 2)$ und der (2×2) Rekonstruktion als auch mit einer Oberfläche mit (1×1) Struktur. Wir können diese Rekonstruktionen ineinander umwandeln, indem wir Strontium oder Titan aufdampfen und in Sauerstoffatmosphäre ausheilen. Rekonstruktionen werden üblicherweise als geordnete Sauerstoff-Fehlstellen, als Strontium-Adatome oder als TiO_2 Doppelschicht beschrieben. Die Modelle für die $c(4\times 2)$ und die (2×2) Oberflächen-Rekonstruktionen zeigen jeweils eine identische Oberflächenstöchiometrie. Dies steht im Widerspruch zu unseren Resultaten.

Diese Arbeit wurde teilweise vom ERC Advanced Grant "Oxide Surfaces" unterstützt.

Contents

1	Introduction	5
2	Strontium Titanate (SrTiO₃, STO): General Description and Literature Review	6
2.1	Literature Review	7
3	Experimental Methods and Setup	11
3.1	UHV System	11
3.2	Experimental Techniques	12
3.2.1	Low Energy Electron Diffraction (LEED)	13
3.2.2	X-Ray Photoelectron Spectroscopy (XPS)	17
3.2.3	Scanning Tunneling Microscopy (STM)	19
3.2.4	Ion Scattering Spectroscopy (ISS)	24
3.3	Synchrotron-based Photoemission (UPS, XPS) and X-ray Absorption Spectroscopy (XAS)	25
3.4	Sample Preparation	30
4	The SrTiO₃(110) Surface	34
4.1	UPS on SrTiO ₃ (110) (4×1)	34
4.2	Sr Adatoms on the SrTiO ₃ (110) (4×1) Reconstructed Surface	38
4.3	Thermal Stability of the Sr Adatoms	41
4.4	XAS on SrTiO ₃ (110) (4×1)	44
5	The SrTiO₃(001) Surface	48
5.1	SrTiO ₃ (001) - Deposition of Sr and Ti	48
5.2	Discussion of Experiments and Structure Models Proposed in the Literature	62
6	Summary and Conclusions	64
	Appendix A STM Scanner Repolarization	68

This thesis focuses on the (001) and (110) surfaces of strontium titanate (SrTiO_3 , often called: STO), a ternary transition metal oxide in the cubic perovskite structure.

1 Introduction

Transition metal oxides are compounds composed of oxygen atoms bound to transition metal atoms. Due to the "progressive filling of shells of d orbitals" [1], transition metal oxides show a huge variety of chemical and physical properties: high/low melting points, color, insulating/metallic conductance [2]; metal-insulator transitions upon pressure or doping [3]; superconductivity (low T_c [4] or high T_c [5]). All of these properties arise from the nature of the bulk of the transition metal oxides.

However, also very interesting phenomena occur on the surfaces of transition metal oxides: While the first promising experiments on the photolysis of water, i.e., the splitting of water into oxygen and hydrogen, were already conducted in 1972 (using TiO_2 as the anode material [6]), research on this topic is still ongoing and attracts much interest, as seen in the studies of Yin et al. in 2004 (achieving a high solar conversion efficiency using n-type doped SrTiO_3 as the anode material) [7]. Furthermore, metal oxide surfaces are sensitive to the contact with different gases. It was found that the conductivity, capacitance, etc. of the metal oxide surface eventually may change, when in contact with gases such as CO , H_2 , CH_4 or O_2 [8].

As a prototypical ternary transition metal oxide with the perovskite crystal structure, we have studied the surface properties of strontium titanate. SrTiO_3 attracts much interest for several reasons: In the field of growing superconducting thin films (e.g., $\text{YBa}_2\text{Cu}_3\text{O}_{7-\delta}$ cuprate-based thin films), its similar physical and structural properties make it a favorable substrate for the growth of these high- T_c superconductors [9]. As already mentioned, it is also a promising material for the photon-induced splitting of water (photolysis). Highest solar conversion efficiency has been achieved with SrTiO_3 as the anode material [7]. Furthermore, there has recently been the discovery of a two-dimensional electron gas (2DEG) at SrTiO_3 surfaces [10] and interfaces to other perovskites, e.g., $\text{LaAlO}_3/\text{SrTiO}_3$ [11]. The phenomenon of the metallic interface between two insulators ($\text{LaAlO}_3/\text{SrTiO}_3$) in particular may pave the way to the field of oxide electronics [12].

It is clear that a control of the geometric and electronic structure of SrTiO_3 surfaces is of essential importance to make it available for all of these applications.

2 Strontium Titanate (SrTiO_3 , STO): General Description and Literature Review

At room temperature strontium titanate crystallizes in the ABO_3 cubic perovskite structure with a lattice parameter of $a_{\text{STO}}=3.905 \text{ \AA}$ [13] and formal ionic charges of Sr^{2+} , Ti^{4+} , and O^{2-} . The unit cell of strontium titanate is shown in figure 1 with a titanium ion in the cube center, strontium ions at the cube corners, and oxygen ions at the cube face centers. In STO, titanium is coordinated octahedrally by 6 oxygen ions, and each strontium ion is surrounded by eight TiO_6 octahedra, which results in a 12-fold coordination for strontium.

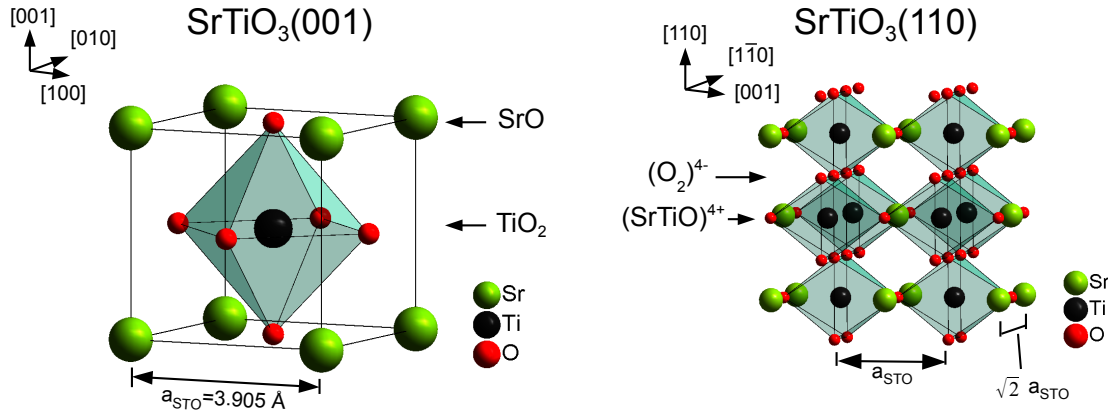


FIGURE 1: Left: Unit cell of SrTiO_3 with titanium in the cube center, strontium at the cube corners, and oxygen at the cube face centers. Titanium is 6-fold, strontium is 12-fold coordinated. Right: SrTiO_3 stacking along the $[110]$ direction. It consists of alternating charged layers of SrTiO^{4+} and O_2^{4-} . Therefore the (110) surface is a polar surface.

Along the $\langle 100 \rangle$ crystallographic directions, strontium titanate is built up of alternating stacks of strontium oxide (SrO) and titanium dioxide (TiO_2) (see fig. 1). Therefore by cleavage, one would expect a (1×1) bulk-terminated surface with both, SrO and TiO_2 areas with one half unit cell of SrTiO_3 step height. Because SrTiO_3 does not cleave well, a surface prepared this way only shows weak (1×1) Low Energy Electron Diffraction (LEED) spots [14]. By considering the number of bonds for each atom in SrTiO_3 (Sr: bulk 12, surface 8; Ti: bulk 6, surface 5) "one could conclude that the TiO_2 surface is more stable, since relatively fewer bonds have to be broken at the surface" [15]. However, cleavage leads to two pieces, each side either being

SrO or TiO₂ terminated. Kawasaki et al. showed that the SrO layers can be removed by chemical etching, which leads to TiO₂ terminated surfaces with one unit cell step height [16].

Along the <110> directions, SrTiO₃ is built up of alternating charged layers of SrTiO⁴⁺ and O₂⁴⁻. Therefore the (110) surface is a polar surface, which has to reconstruct in order to be stable.

Most groups use mechanically polished and chemically etched SrTiO₃ samples. One can produce atomically flat terraces simply by sputtering with argon ions for cleaning and heating to high temperatures (usually in an oxygen environment) for ordering and flattening the surface again.

2.1 Literature Review

SrTiO₃ surfaces have already been investigated intensively. The following tables 1 to 3 show the work of different groups investigating SrTiO₃(001) [17–31], (110) [22, 32–34] and (111) [35–37] surfaces. The first column shows the observed reconstruction, the following columns show the preparation procedures applied. It can be seen that the preparation procedures consist of a precise control of the parameters for sputtering and annealing and that the sample history can also be important. A much more easy and convenient way to tune the surface reconstructions on the SrTiO₃(110) surface was shown by Wang et al. [34]. They showed that the reconstructions can be transformed reversibly into each other simply by depositing a certain amount of strontium or titanium and annealing in oxygen. The phase diagram will be discussed later in section 4.

Reconstructions on the SrTiO ₃ (001) surface				
	Sample preparation	Annealing Temp. [K]	Annealing atmosphere	Reference
(1×1)	Sputtered	873 - 1100	UHV or 10 ⁻⁶ mbar O ₂	[17–20, 22, 23, 31]
(2×1)	Sputtered	873 - 1100	UHV or atmospheric O ₂	[19–24, 26]
(2×2)	Sputtered	900 - 1473	UHV or 10 ⁻⁵ mbar O ₂	[17, 19, 20, 25]
c(4×2)	(2×1) + Sputtering	950 - 1673	UHV or atmospheric O ₂	[21, 23, 25, 26]
c(4×4)	(2×1)	1173 - 1673	UHV	[23, 25]
(4×4)	c(4×4)	1423	UHV	[25]
c(6×2)	Sputtered	1073 - 1373	atmospheric O ₂	[22, 24, 26–28]
(6×2)	(2×1) + Sputtering	1073 - 1373	UHV	[21]
($\sqrt{5} \times \sqrt{5}$ R26.6°)	(4×4)	1073 - 1473	UHV	[25, 29–31]
($\sqrt{13} \times \sqrt{13}$ R33.7°)	($\sqrt{5} \times \sqrt{5}$ R26.6°)	1073 - 1573	UHV or atmospheric O ₂	[22, 25]

TABLE 1: Sample preparation procedures used by different groups to obtain reconstructed surfaces of SrTiO₃(001).

Reconstructions on the SrTiO ₃ (110) surface				
	Sample preparation	Annealing Temp. [K]	Annealing atmosphere	Reference
(2×5)	Sputtered	1233	UHV	[32]
(3×4)	Sputtered	1173	UHV	[32]
(4×4)	Sputtered	1173 - 1393	UHV	[22, 32]
(4×7)	Sputtered	1233	UHV	[32]
(6×4)	Sputtered	1173	UHV	[32]
c(2×6)	Annealing	1573	UHV	[33]
(n×1) (n=3,4,5,6)	Sputtered and Ti/Sr deposition	1273	10 ⁻⁶ mbar O ₂	[34]
(m×4) (m=2,6)	Sputtered and Ti/Sr deposition	1273	10 ⁻⁶ mbar O ₂	[34]
(1×1) (l=4,5)	(4×1) + Ti deposition	923	10 ⁻⁶ mbar O ₂	[34]

TABLE 2: Sample preparation procedures used by different groups to obtain reconstructed surfaces of SrTiO₃(110).

Reconstructions on the SrTiO ₃ (111) surface				
	Sample preparation	Annealing Temp. [K]	Annealing atmosphere	Reference
(1×1)	Polished	1073	UHV	[35]
(4×4)	Polished	1473	UHV	[35]
($\sqrt{7} \times \sqrt{7}$ R19.1°)	Sputtered	1123	UHV	[36]
($\sqrt{13} \times \sqrt{13}$ R13.9°)	Sputtered	1123	UHV	[36]
(3×3)	Sputtered	1423	10 ⁻⁶ mbar O ₂	[37]
(5×5)	Annealing	1273	UHV	[37]
(6×6)	Sputtering	1223	UHV	[37]

TABLE 3: Sample preparation procedures used by different groups to obtain reconstructed surfaces of SrTiO₃(111).

3 Experimental Methods and Setup

Experiments in surface physics are conducted in an ultra high vacuum (UHV) environment, i.e., in a pressure of less than 10^{-9} mbar. One can imagine a surface in contact with a gas of pressure p . For an ideal (i.e., very diluted) gas the impinging rate Z_A of the gas molecules onto the surface is directly proportional to the pressure (using Boltzmann statistics):

$$Z_A = \frac{n\bar{v}}{4} = \frac{p}{\sqrt{2\pi mkT}} \quad (1)$$

n is the particle density, \bar{v} the mean velocity of the gas particles, p the pressure, m the mass, k the Boltzmann constant, and T the temperature. Therefore in an atmosphere of 10^{-6} mbar, a surface gets covered by one monolayer of gas molecules within one second [38] (assuming a sticking coefficient of 1). Ultra high vacuum is therefore essential for keeping well defined surfaces clean for the time needed for analysis.

3.1 UHV System

To achieve ultra high vacuum, usually several different pumping stages are used. Initially, roughing pumps evacuate the system to a pressure of about 10^{-3} mbar. Scroll pumps are employed in the present work, which use interleaving scrolls where one scroll is fixed and the other scroll is moving in a circular motion without rotation. Gas is trapped between the scrolls and gets pumped to the exhaust. The low-pressure side of the scroll pumps is connected to the exhaust of the so-called turbo-molecular pumps (turbo pumps). After a pressure of 10^{-3} mbar is achieved, the turbo pumps start spinning to full speed (1000-1500 rpm). These high-vacuum pumps work with several rotor/stator pairs mounted in series. The rotor blades spin with a velocity comparable to the mean velocity of the gas molecules. A collision with a rotor blade transfers momentum to each gas molecule in a favored direction, i.e., to the scroll pump.

A vented chamber cannot be pumped quickly. The residual pressure is dominated by water molecules desorbing off the chamber walls. Pumping a chamber in this condition may take several weeks to finally achieve a pressure in the order of 10^{-9} mbar. To speed up the pumping procedure dramatically, UHV chambers are heated up to around 150° C while the turbo pumps run simultaneously. After this so-called bake-out, the turbo pumps are able to keep the pressure below 10^{-9} mbar. To decrease the pressure even more, ion getter pumps are utilized. High-energy electrons are created and trapped inside the pump. Residual gas atoms are ionized when hit by these electrons.

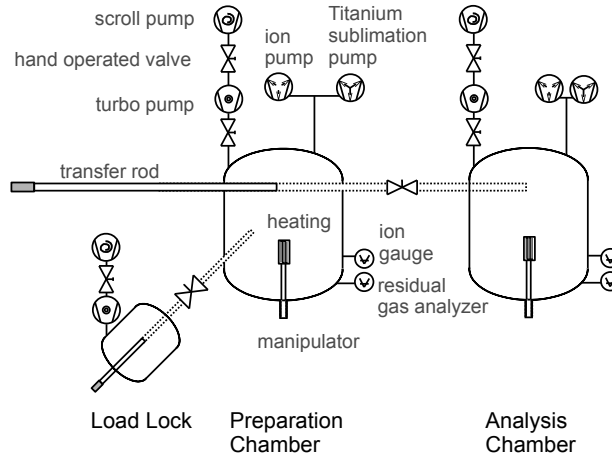


FIGURE 2: A schematic of the vacuum system used for this work: Both chambers, for analysis and for preparation, are equipped with turbo-, ion- and titanium sublimation-pumps to achieve ultra high vacuum (10^{-10} mbar to 10^{-11} mbar). For introducing samples quickly into the UHV, a load lock with a turbo pump is attached.

The ions then get accelerated towards a chemically active getter material (usually titanium) and are stored there. A strong magnetic field prolongs the travel distance of the electrons and therefore increases the probability of ionization. Additional titanium sublimation pumps (TSP) can be used to improve the pumping speed of the system even more. A high current is passed through a titanium rod and heats it until some of the titanium evaporates and builds a thin film on the chamber walls close by. Since titanium is a chemically very reactive material, residual gas molecules eventually get stored when hitting the fresh titanium film. Finally a pressure below 10^{-10} mbar can be established, which keeps surfaces clean in the order of hours. For information on UHV technology see the lecture notes of Prof. Schmid [38]. Figure 2 shows a schematic of the vacuum system of the experimental setup used in this work.

3.2 Experimental Techniques

The experimental system consists of two ultra high vacuum chambers. In the preparation chamber, the pressure is kept below 10^{-9} mbar. This chamber is used for preparation procedures, such as sputtering with argon ions, titanium or strontium deposition, and annealing in oxygen atmosphere ($p_{\text{O}_2} = 10^{-6}$ mbar). The analysis chamber keeps the pressure constant in the order of 10^{-11} mbar and is used for analysis, such as Low Energy Elec-

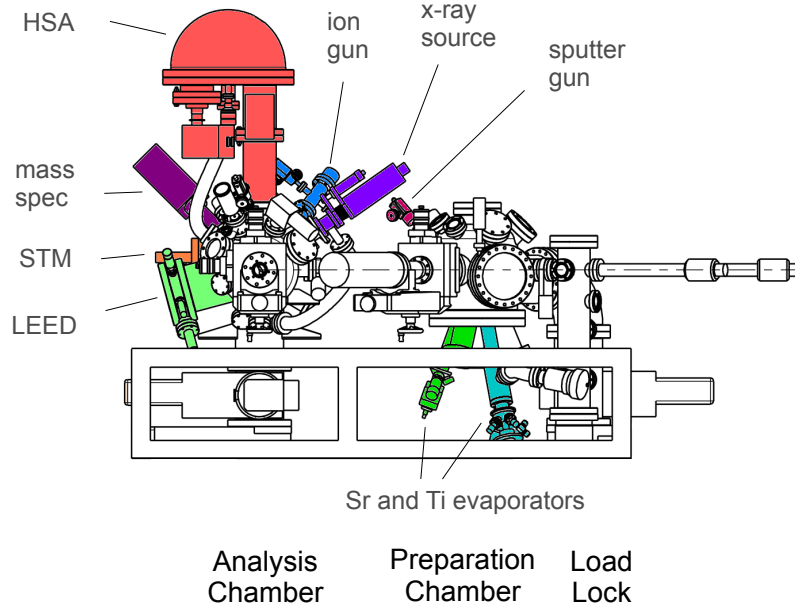


FIGURE 3: Schematic of the experimental setup. Colors indicate the various tools that were used (abbreviations are explained in the main text). Drawing from SPECS GmbH.

tron Diffraction (LEED), Scanning Tunneling Microscopy (STM), X-Ray Photoelectron Spectroscopy (XPS), and Ion Scattering Spectroscopy (ISS). Figure 3 shows a drawing of the system (taken from the system proposal of the company SPECS GmbH), the experimental tools are indicated in colors.

3.2.1 Low Energy Electron Diffraction (LEED)

LEED is a commonly used technique to reveal periodic structures of a surface. Low-energy electrons, i.e., electrons with an energy of around 100 eV, exhibit a de Broglie wavelength of a few Ångström, which is comparable to interatomic distances:

$$p = \frac{h}{\lambda} \Rightarrow \lambda[\text{Å}] \approx \sqrt{\frac{150.4}{E[\text{eV}]}} \quad (2)$$

Incident low-energy electrons therefore satisfy the diffraction condition (equation 3 and figure 4) and show an angle dependent variation of the back-scattering intensity (first shown experimentally by Davisson and Germer in 1927 [39]):

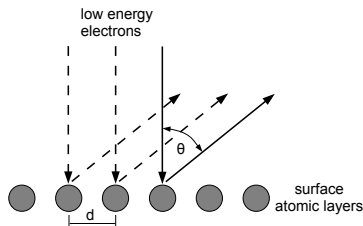


FIGURE 4: Scattered electrons experience positive interference if the path difference of the scattered electron waves is an integer value of the wavelength. d is the spacing of the lattice, θ the scattering angle.

$$n \lambda = d \sin \theta \quad (3)$$

Figure 5 shows a schematic of a typical LEED setup. Electrons are emitted by a hot cathode (on negative potential) and accelerated and focused onto the sample. The back-scattered and diffracted electrons then have to pass several grids. To suppress deflecting electric fields, the sample as well as the first grid are grounded. The second grid lies slightly below the negative acceleration voltage, so that only elastically backscattered electrons are able to pass. The third grid is again on ground and the fluorescent screen itself lies on positive high voltage (around 5 kV). Therefore only elastically back-scattered electrons are able to pass the grids and may produce a pattern on the screen. The inelastic mean free path of electrons traveling through matter shows a general energy-dependent behavior: For most materials, it has a minimum at electron energies of around 10-100 eV (compare figure 6). Because of this behavior and the grid repelling inelastically scattered electrons, LEED is a very surface sensitive technique. In a qualitative analysis, the diffracted pattern on the screen is interpreted as the reciprocal structure of the surface under investigation. This can be understood with the following considerations (derivation in analogy to reference [41]): The electron source is far away from the sample surface. Therefore, the incident electrons can be described as plane waves:

$$\Psi(\vec{r}) \propto e^{i\vec{k}_0 \cdot (\vec{r} + \vec{r}_{m,n})} \quad (4)$$

\vec{k}_0 is the incident wave vector, \vec{r} is the vector from the source into the scattering region and $\vec{r}_{m,n}$ is the vector from \vec{r} to each scattering point. Every atom in a scattering event can be seen as a point source of an outgoing (scattered) spherical wave (Huygens-Fresnel principle) stimulated by the incoming wave. The wave-function after scattering at one lattice point, seen at the detector

far away from the sample, therefore is:

$$\Psi' \propto e^{i\vec{k}_0 \cdot (\vec{r} + \vec{r}_{m,n})} \cdot \rho(\vec{r}_{m,n}) \cdot \frac{e^{ik'|\vec{r}' - \vec{r}_{m,n}|}}{|\vec{r}' - \vec{r}_{m,n}|} \quad (5)$$

$(\vec{r}' - \vec{r}_{m,n})$ is the vector from a scattering point to the detector and $\rho(\vec{r}_{m,n})$ is the density of the scattering points. For a fixed detector position, the scattered wave vector \vec{k}' points into the same direction as $\vec{r}' - \vec{r}_{m,n}$, hence one can transform:

$$k'|\vec{r}' - \vec{r}_{m,n}| \rightarrow \vec{k}'(\vec{r}' - \vec{r}_{m,n}) \quad (6)$$

Also since the detector is sufficiently far away from the sample, one can write $|\vec{r}' - \vec{r}_{m,n}| \rightarrow r'$. Now by integrating over all lattice points, one finds [41] for the scattering intensity ($I(\vec{K}) = |\Psi|^2$, with $\vec{K} = \vec{k}_0 - \vec{k}'$):

$$I(\vec{K}) \propto \left| \int \rho(\vec{r}_{m,n}) e^{i\vec{K} \cdot \vec{r}_{m,n}} d\vec{r}_{m,n} \right|^2 \quad (7)$$

The intensity on the screen is proportional to the Fourier transformation of the real space lattice. It shows the so-called reciprocal lattice. One can visualize the elastic diffraction by constructing the Ewald sphere (see figure 5). By considering elastic scattering only, all scattered wave vectors lie on a sphere ($|\vec{k}_0| = |\vec{k}_i|$). The real-space two-dimensional lattice can be interpreted in reciprocal space as rods arranged in a periodic order. Whenever a so-called truncation rod intersects the Ewald sphere, diffraction into this direction shows constructive interference ($\Delta\vec{k}_{\parallel} = \vec{G}$, with \vec{G} being a reciprocal lattice vector). The condition $\Delta\vec{k}_{\parallel} = \vec{G}$ for constructive diffraction is derived by representing the density of scattering points $\rho(\vec{r}_{m,n})$ in a Fourier series:

$$\rho(\vec{r}_{m,n}) = \sum_{\vec{G}} \rho_{\vec{G}} e^{i\vec{G} \cdot \vec{r}_{m,n}} \quad (8)$$

The integral of the intensity on the screen then only gives considerable contribution if $\vec{G} = \vec{K}$.

Figure 7 shows a typical LEED image of a (2×2) reconstructed surface. The reciprocal unit cell of the super structure (indicated by the vectors b_1^* and b_2^*) always lies within the reciprocal (1×1) cell (indicated by the vectors a_1^* and a_2^*). A reciprocal lattice vector is produced by: $a^* = \frac{2\pi}{a}$. a is the real space lattice vector. Scattering on the (1×1) subsurface structure usually produces the most bright spots, called $(1,0)$ $(0,1)$ and $(1,1)$ spots in the upper right quadrant of the screen (notation in Miller indices [41]). The specular spot $(0,0)$ would be in the center of the screen and is covered by the

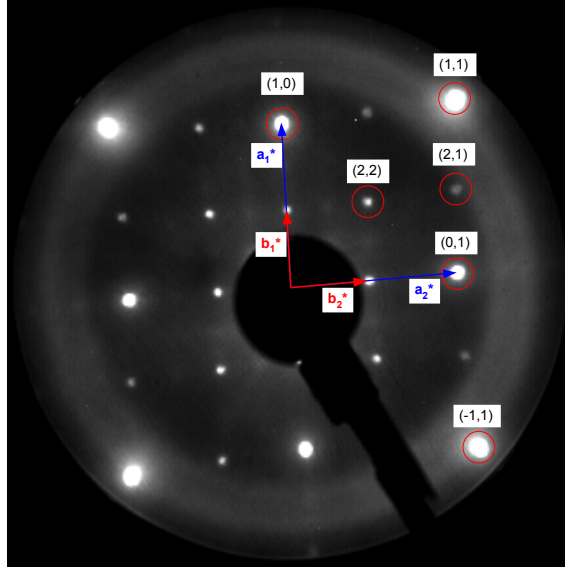


FIGURE 7: Typical LEED image of a (2×2) reconstructed surface: The pattern reflects the reciprocal space, therefore the higher order pattern exists within the reciprocal (1×1) unit cell. Image taken at 69 eV. Notation in Miller indices.

shadow of the electron gun. Within this reciprocal unit cell, a higher order reciprocal structure exists. In this example, a (2×2) pattern is visible. If the phase information would also be visible, the reciprocal structure could be completely transformed back into the real space structure by Fourier transformation. Usually, with the help of software, e.g., LEEDpat [42], LEED patterns are simulated and compared to the experiment to find the right interpretation.

In the present work, a SpectaLEED with a micro-channel plate (MCP) from Omicron Nanotechnology was used. The LEED images have been captured by a CCD camera and the image capturing software of k-Space Associates Inc..

3.2.2 X-Ray Photoelectron Spectroscopy (XPS)

XPS is a powerful technique to reveal the elemental composition of a sample and which gives rise to information about the chemical environment of the atoms. The physical basis of this technique is the photoelectric effect, first explained by Einstein in 1905 [43]: A photon with energy $E = h\nu$ can be absorbed by an electron bound in an atom. If the photon energy exceeds the binding energy E_B of this electron and the work-function Φ of the sample, the

electron can leave the sample with a kinetic energy E_{kin} given by equation 9. Figure 8 shows a schematic of the process of photo excitation of a core level electron from a semiconductor.

$$E_{kin} = h\nu - E_B - \Phi \quad (9)$$

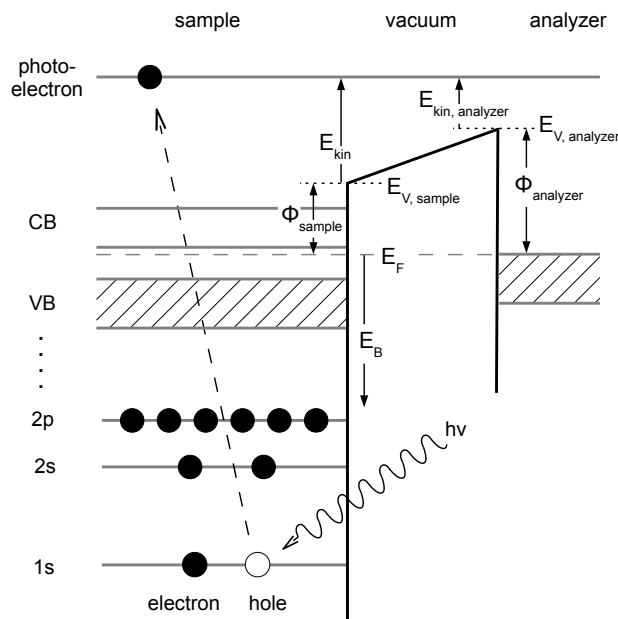


FIGURE 8: Schematic of the mechanism leading to electron emission in XPS: An incoming photon, with energy $E = h\nu$, excites an electron. Overcoming the binding energy in the atom and the work-function of the sample leads to the emission of the electron. Image adapted from reference [38].

In an XPS experiment, the sample is connected to ground to prevent charging. In most cases the analyzer is grounded as well. The kinetic energy measured is then related to the vacuum level of the analyzer, i.e., instead of Φ_{sample} , the work function of the analyzer must be considered. Acquiring a spectrum simply means to measure the intensity for a given kinetic energy of the photoelectrons. Since the electron binding energies for each shell of each element are characteristic, an XPS spectrum can be interpreted in terms of elemental and chemical composition. Typically an x-ray tube is used as the source. Bombarding an aluminum or magnesium target with high energy electrons ($E \approx 15 \text{ keV}$) produces continuous and characteristic x-rays. Continuous radiation is produced by the deflection (acceleration)

of the electrons (Bremsstrahlung) whereas characteristic x-rays are emitted if a core hole (electron-electron scattering) gets refilled by electrons from higher orbitals. The so-called K_α lines (refilling of a K-orbital hole by an L-orbital electron) show the highest intensity and are used in XPS experiments ($E_{Mg\ K_\alpha} \approx 1253.6\text{ eV}$ and $E_{Al\ K_\alpha} \approx 1486.7\text{ eV}$).

Usually a hemispheric energy analyzer (HSA) is used to measure the kinetic energy of the electrons (see figure 9). The geometry as well as the applied voltages of the hemispheric analyzer only allow electrons having one specific kinetic energy, the so-called pass energy, to pass the hemispheres. Photo-emitted electrons get retarded to the pass energy and focused into the entrance slit (S_1), then run through the analyzer and get focused into the exit slits (S_2). Right after the exit slits, the electrons get detected by several channeltrons. The multiple slits and channeltrons also allow electrons exhibiting slightly higher or lower kinetic energies to be detected. This results in a higher counting rate and therefore in higher statistics.

In the present work, a DAR400 x-ray source from Omicron Nanotechnology and a Phoibos 100 hemispherical analyzer from SPECS GmbH have been used.

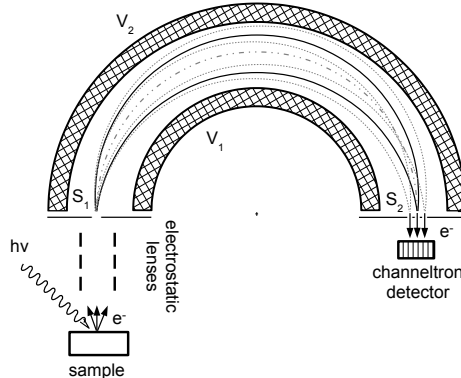


FIGURE 9: Cross section of a hemispherical energy analyzer (HSA): Photoelectrons leaving the sample get focused in the slit S_1 . With the appropriate energy (pass energy), electrons get focused from slit S_1 to S_2 . When several exit slits and channeltrons are used in the detector, a small energy range can be scanned at the same time. Image adapted from reference [44].

3.2.3 Scanning Tunneling Microscopy (STM)

STM is a powerful technique to visualize the geometric and electronic structure of a surface in real space. The quantum-mechanical tunnel effect enables

electrons to flow between a tip and a sample, even if there is a potential barrier between them. For an electron moving in \vec{x} direction with an energy E greater or less than a potential V , the solution Ψ of the time independent Schrödinger Equation (equation 10) can be written as:

$$\left(-\frac{\hbar^2}{2m}\Delta + V\right)\Psi = E\Psi \quad (10)$$

$$\Psi \propto \begin{cases} e^{i\vec{k}\cdot\vec{x}} & \text{for } E > V \\ e^{-\kappa\cdot x} & \text{for } E < V \end{cases} \quad (11)$$

$E = \hbar^2 k^2/2m$ is the kinetic energy of the electrons, m the electron mass, V the potential and κ is a constant proportional to E , V and m . There is an exponentially decreasing but finite electron density ($\rho(x) = |\Psi(x)|^2$) inside the classically forbidden barrier, which is the basis of the quantum-mechanical tunnel effect (see figure 10).

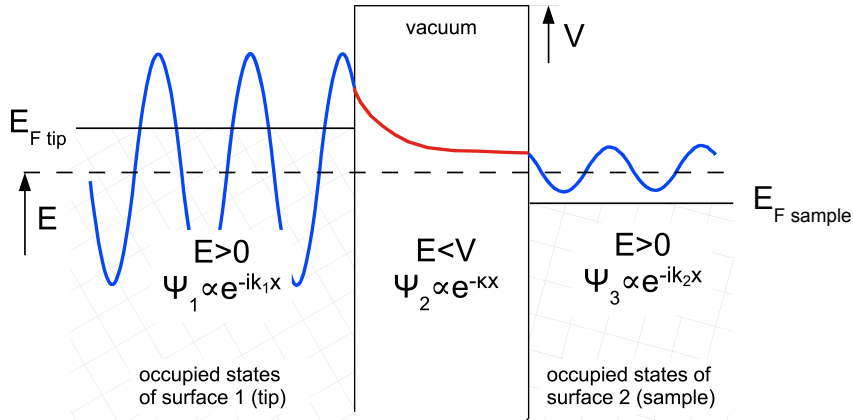


FIGURE 10: If an electron with energy E travels towards a barrier of height V , there is a finite probability that the electron can overcome this barrier by tunneling through it. Coming from the left, the electron can be described as a plane wave (with energy $E > 0$). Inside the classically forbidden region, the electron wave function is exponentially decreasing. After the barrier, the wave function eventually still exists with a much lower amplitude, but the same energy. Image adapted from reference [45].

Using this effect for imaging surfaces in real space was first published by Binnig and others in 1982 [46]. If a potential is applied between a tip and a conducting sample, and the tip is approached sufficiently close to the surface, electrons eventually start to flow. The potential barrier in this case is dependent on the voltage applied and the distance between the tip and the sample. A common convention for the polarity of the bias is that the tip is

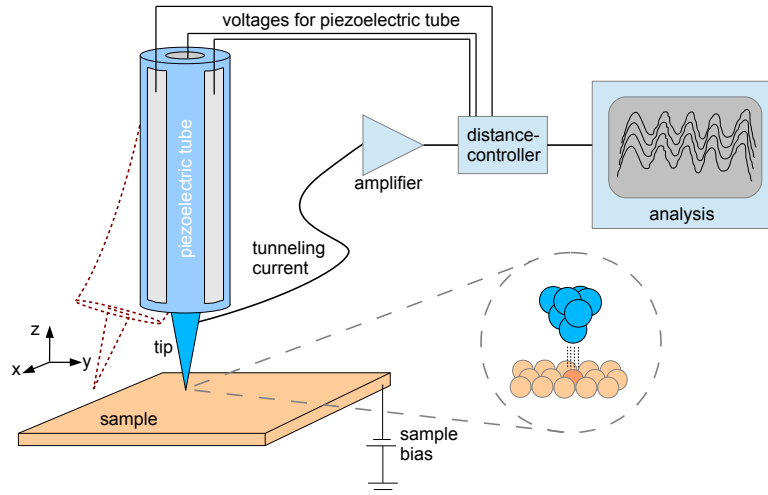


FIGURE 11: Schematic view of a typical STM setup: The tip is mounted on a piezoelectric tube, which is approached to the sample until a tunneling current is measured. The tip can be scanned across the surface by applying voltages to the piezo tube. A feedback loop regulates the height of the tip. Image adapted from [38].

on virtual ground and the bias voltage is the sample voltage [47]. Therefore with positive bias, electrons are tunneling from occupied states of the tip to unoccupied states of the sample and vice versa for negative biasing. Since the probability of tunneling shows an exponential dependence, variations in the distance of around 1 Ångström result in a change of the tunneling current by a factor of 5 to 10 [38].

A typical STM setup is shown in figure 11. An electrochemically etched tungsten tip is mounted on a piezo scanner tube. The scanner voltages are regulated by the distance- and scanning-controller unit. If the tip is sufficiently close to the sample and a current is flowing, the tip is scanned across the xy -plane. The distance controller continuously uses the tunneling current as a feedback and regulates the height of the tip in order to keep the tunnelling current constant (so-called Constant Current Mode). Assuming an s -wave at the tip, the tunnelling current is directly proportional to the density of states (initial and final states) and the tip follows lines of equal density of states of the sample [47] (see figure 12). This mode of operation also ensures that the tip is not easily crashed into something protruding out of the sample surface. By taking the values applied by the controller (x -, y - and z -voltage) a topographic image of the surface electronic structure can be visualized. We used the software ImageJ [48] with plug-in's and macros written by Prof. Schmid, which provide all tools necessary to analyze

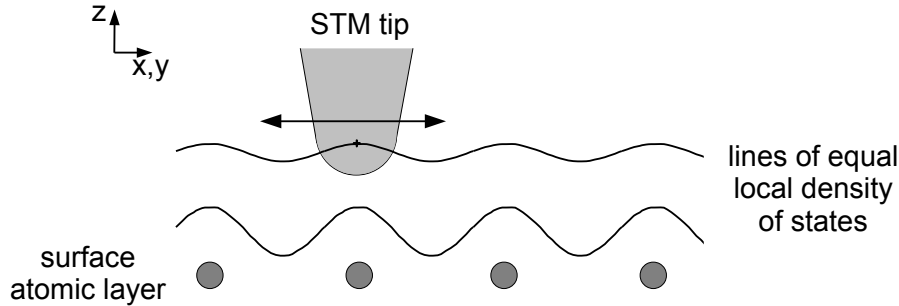


FIGURE 12: In the constant current mode, the tip is following lines of constant local density of states. Image adapted from [38].

STM images (e.g., 'background subtraction', 'measure periodicity', 'linear undistortion', 'fast Fourier transformation'). The STM tip is prepared ex situ, which means that atmospheric water and adsorbates sit most likely on the tip or form an insulating layer. To remove all adsorbates, the tip can be sputtered with Ar^+ ions. To prevent the ions from hitting also the piezo ceramic scanner tube, a so-called tip sputtering plate is inserted into the STM. This plate looks exactly like a sample plate, only with a tiny hole in its center. The tip is approached to this hole, in the best scenario it goes through the hole, and can then be sputtered safely. The STM used in this work is of type STM 150 Aarhus by SPECS GmbH.

STM Scanner Depolarization and Calibration The scanner tube of the STM consists of a piezo-electric tube with one electrode in its center and for each scanning direction (x,y) two electrodes at opposing sides (see figure 11). The polarization of the piezo material is of central importance for the moving of the scanner [49]. The scanner is usually permanently radially polarized. A given voltage on its electrodes leads to an equal displacement of the scanner tube into both directions (x,y). Local high temperatures or local charging, e.g., argon ions hitting the scanner tube during tip sputtering, can lead to a local change in polarization or even depolarization. This would cause a different displacement for a given voltage in the direction of different polarization. This has been the case in the first half of this study. The STM images all are skewed and a shear angle of about 20-35 degrees had to be applied in image processing for undistortion. This was most likely due to a polarization problem and we therefore re-polarized the scanner tube. The procedure of re-polarization is described in the Appendix.

Distances measured by the STM are always relative values and have to be referred to a structure with known distances. Usually the calibration value is an input for the STM software. We have not been able to calibrate the images directly within the STM software. Therefore we have set the scale in image-processing (ImageJ) according to the Au(111) lattice parameter measurements. Figure 13 shows an STM image of the Au(111) surface with atomic resolution. This surface has been used to calibrate the scanner. The nearest-neighbor distance of gold is 2.884 \AA [50]. The measured distance is compared to this value and the calibration is applied to subsequent STM images. Table 4 shows measured values of the Au(111) lattice parameter and the relative error for STM images acquired on different days. The relative error has been used to calibrate the STM images.

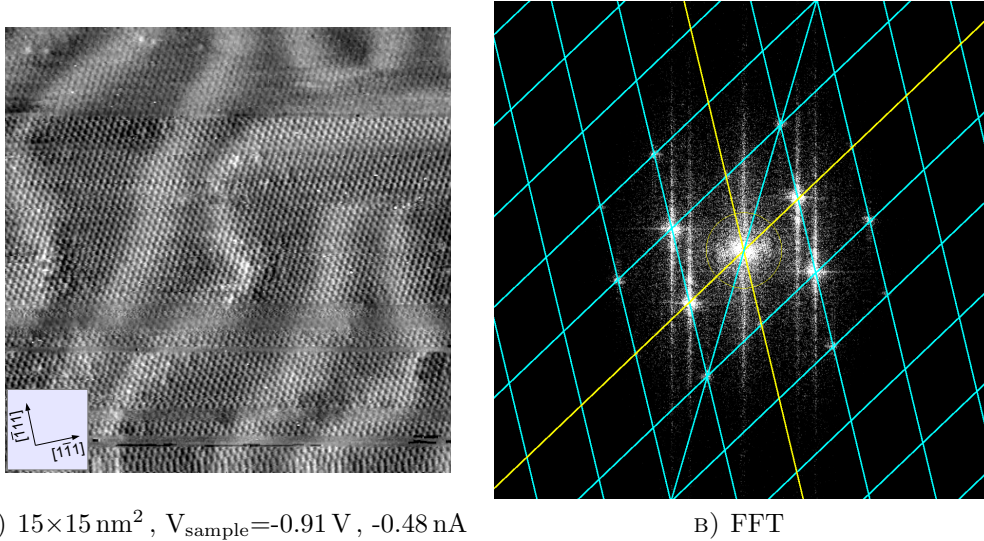


FIGURE 13: A) Small scale STM image of the Au(111) surface with atomic resolution: The well-known herringbone reconstruction is also visible. B) Fast Fourier transformation (FFT) of the image in A) overlaid with the grid to measure the lattice constant. Since the lattice constant of gold is well known, this can be used to calibrate the STM scanner.

STM Scanner Calibration ($a_{\text{Au}(111)} = 2.884 \text{ \AA}$)		
date.file	measured $a_{\text{Au}(111)}$ [\AA]	$\frac{\text{measured } a_{\text{Au}(111)}}{\text{real } a_{\text{Au}(111)}}$
1126.mul2	2.422	0.84
1127.mul16	2.282	0.79
1212.mul4	2.236	0.78
1219.mul4	2.226	0.77
0107.mul1	2.226	0.77

TABLE 4: Measured values for the Au(111) lattice parameter and the relative error according to the real value.

3.2.4 Ion Scattering Spectroscopy (ISS)

ISS is an analytical technique used to probe the elemental composition of the first few atomic layers of a sample. When bombarding a surface with low energy ions, the probability of neutralization is high but eventually the ions undergo elastic scattering with the surface atoms and get back-scattered in a defined manner. The scattering behavior of the ions is governed by the equations of momentum and energy conservation and one can derive, for a given scattering geometry, a solution of the kinetic energy of the ions after scattering:

$$E_1 = E_0 \left(\frac{m_1 \cos \theta \pm \sqrt{m_2^2 - m_1^2 \sin^2 \theta}}{m_1 + m_2} \right)^2 \quad (12)$$

E_0 and E_1 are the kinetic energies before and after the scattering event, respectively, m_1 is the ion mass, m_2 is the target atom mass and θ is the scattering angle. In our experiment, we only detect ions scattered into the direction towards the analyzer (see figure 14). Therefore the scattering angle is fixed at $\theta=137^\circ$. The ion intensity is then measured with the hemispherical analyzer. By plotting the ion signal intensity versus the kinetic energy of the scattered ions, one can determine at which atom the ions got back-scattered. Since the probability of neutralization is high, this method is very surface sensitive.

An ion source of type IQE 11/35 with a Wien filter from SPECS GmbH and the Phoibos 100 analyzer have been used to perform ISS measurements.

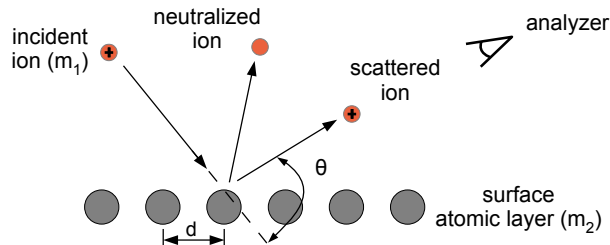


FIGURE 14: Scattering of an ion on a surface atom: The probability of neutralization is high, therefore outgoing ions mostly just scattered at the first atomic layer.

3.3 Synchrotron-based Photoemission (UPS, XPS) and X-ray Absorption Spectroscopy (XAS)

In the course of this diploma thesis, measurements at the I311 beamline at the synchrotron facility MAXLAB in Lund (Sweden) were conducted. Figure 15 shows a schematic of the I311 beamline. High energy electrons inside the MAX II storage ring (operating energy 1500 MeV) are brought into an arrangement of alternating magnetic dipoles (undulator). When experiencing acceleration, e.g., forced in a circular motion, charged particles emit photons (synchrotron radiation). The setting of the undulator (distance of dipoles and strength of magnetic field) allows the selection of the energy of the synchrotron radiation. An optical arrangement of a monochromator grating (G) and mirrors (M1-M5) then monochromatizes the radiation even more and focus the photons onto the sample [51]. The endstation is equipped with a chamber to perform different preparation procedures and an analysis chamber with an SES200 electron spectrometer from VG Scienta. The synchrotron is capable of producing an ultra-high flux of photons (around 10^{12} photons per second) with energies in the range of 40 to 1500 eV. The very good energy resolution of this beamline (light source and analyzer) and the variable photon energy allow to perform high-resolution XPS as well as Ultra-violet Photoelectron Spectroscopy (UPS). Since ultra violet photons are only able to excite electrons from the outermost orbitals of an atom, UPS is well suited to investigate the Valence Band (VB) of a sample. A UPS spectrum directly reflects the energy dependent density of states (DOS). However several effects (momentum conservation, selection rules, and inelastic scattering) alter the shape to finally get a typical UPS spectrum. Figure 16 illustrates the creation of a UPS spectrum of a metal. A typical feature for a metal is the so-called Fermi edge. Since for a metal, the Fermi energy is within an energy band, UV-photons are able to excite electrons up to the Fermi level and then the spectrum shows an immediate decrease. The Fermi edge can be used to

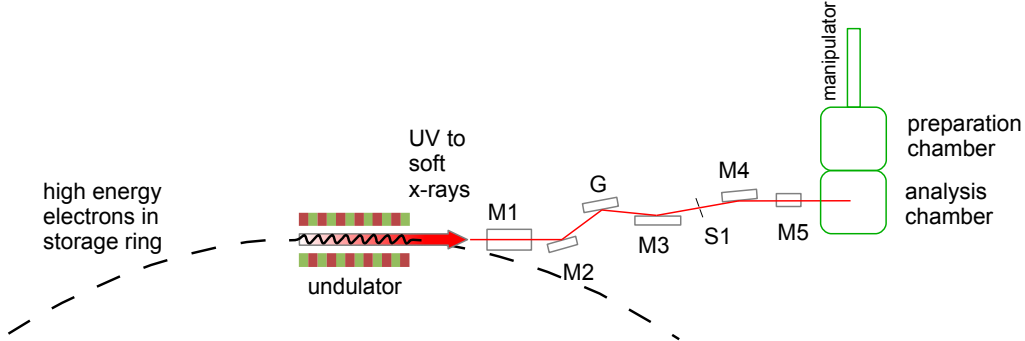


FIGURE 15: The I311 beamline at the MAXLAB in Lund, Sweden: High energy electrons from the synchrotron produce an ultra high flux of photons in the range of 40-1500 eV in the undulator. An optical arrangement of monochromator grating (G) and mirrors (M1-M5) with a slit (S1) energy-select and focus the photons onto the sample. Image adapted from reference [51].

calibrate the energy of the synchrotron radiation. As discussed above the kinetic energy of the photoelectrons measured in the analyzer is given as:

$$E_{kin} = h\nu - E_B - \Phi_{analyzer} \quad (13)$$

$E_B = 0$ at the Fermi level and $\Phi_{analyzer}$ is usually known.

Another powerful technique available at a synchrotron is X-ray Absorption Spectroscopy (XAS). When sweeping the photon energy across a characteristic binding energy of an electron bound in an atom, a typical XAS-spectrum can be produced (see figure 17). The spectrum shows the intensity of absorption versus the incident photon energy. Coming from the left, the photon energy rises until its energy is in resonance with the binding energy of an electron (plus eventually an additional energy gap in semiconductors). The photon is able to excite the electron into the first unoccupied state and the absorption rises dramatically. After the main absorption peak (also called absorption edge), the spectrum flattens out with oscillations. An XAS spectrum is typically divided into three main regions [53]. The dominant feature is called XANES (X-ray Absorption Near Edge Structure) and essentially shows the resonant absorption of a photon by a core shell electron. The next region is referred to as NEXAFS (Near Edge X-ray Absorption Fine Structure) and is related to the chemical environment of the atom under consideration. The third region called EXAFS (Extended X-ray Absorption Fine Structure) is showing oscillations produced by the excited electronic spherical wave being reflected back by the neighboring atoms (see figure 18), and therefore is a

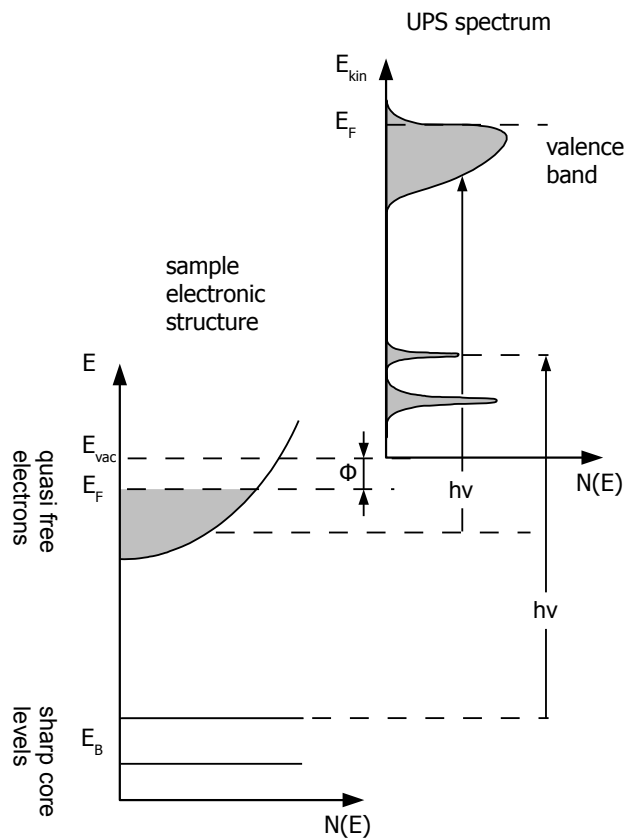


FIGURE 16: Typical UPS spectrum of a metal. Ultra violet photons are only able to excite weakly bound electrons (from the VB). On the left, the density of states for core levels (sharp) and the valence band (approximated as free electrons with \sqrt{E} shape) is shown. On the right is the actual spectrum: Sharp core states get broadened (intrinsic effect). At the Fermi level the intensity decreases immediately. Image taken from reference [52].

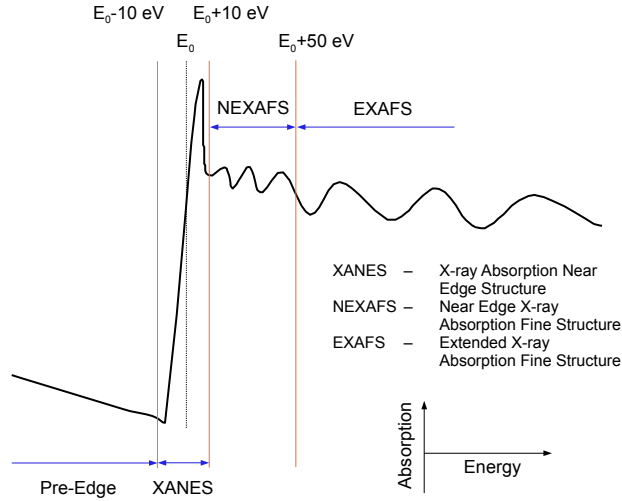


FIGURE 17: Schematic of an absorption spectrum: Photons with sufficient energy get absorbed by core level electrons and the absorption signal increases. Image taken from reference [53].

signature of the local binding character, such as bond lengths. The simplest way to measure the intensity of absorption is to measure the drain current from the ground to the sample. This measurement method is called Total Electron Yield (TEY) and the information consists of all secondary electrons, i.e., inelastically scattered photo- and Auger electrons, excited into the vacuum. The information depth is determined by the escape depth of the electrons (around 5-10 nm). Detecting only electrons emitted through Auger processes, which are related to the atom under investigation, makes the spectrum much more surface sensitive (see figure 19). This comes from the low kinetic energy of Auger electrons (compare figure 6). With this so-called Auger Electron Yield (AEY), XAS information only comes from the first few layers (around 1 nm). Figure 20 shows a schematic view of the absorption of an x-ray photon by a core-level electron. The residual core hole can be refilled by a valence electron, which can give its energy to another valence electron. The second electron is then able to leave the sample and is called Auger electron.

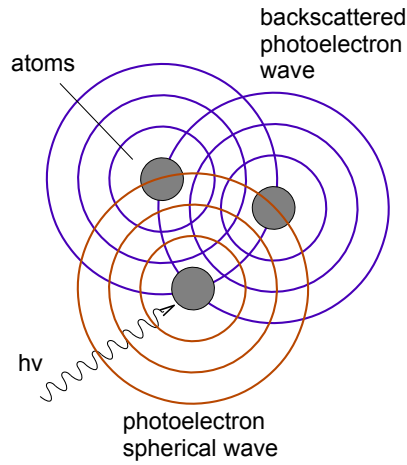


FIGURE 18: The extended x-ray absorption fine structure is caused by a back-scattering of the spherical photoelectron wave from neighboring atoms. This causes interference at the original atom. Image adapted from reference [54].

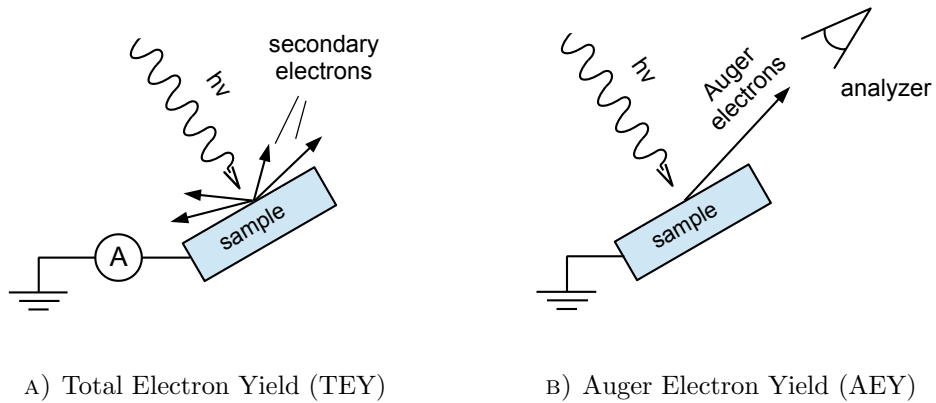


FIGURE 19: Two modes of XAS: A) TEY measures the drain current to the sample. This mode is more bulk sensitive. B) AEY measures the Auger electron intensity. This mode is surface sensitive.

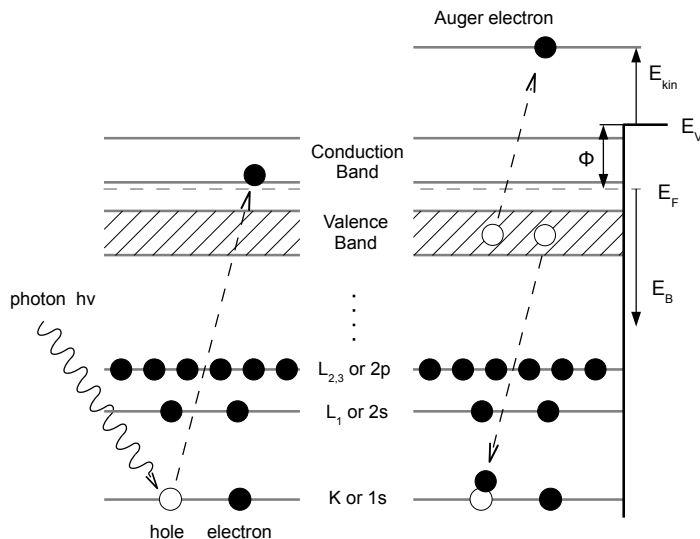


FIGURE 20: Schematic view of the absorption of an x-ray and an Auger process in a semi-conductor: A photon with sufficient energy is able to excite a core-level electron into the first unoccupied states (for a semiconductor: into the conduction band). The highly unstable core-hole gets refilled by an electron from a higher electron level, e.g., the valence band. This electron either emits a photon or this energy is transferred to another VB-electron, which is then able to leave the compound as an Auger-electron. Image in analogy to figure 8.

3.4 Sample Preparation

SrTiO₃ crystals, with a niobium doping of 0.5 wt%, cut and epi-polished so that the polished surface normal is along $\langle 001 \rangle$ and $\langle 110 \rangle$ directions were obtained from MaTeck GmbH. The samples were put into an isopropanol or acetone bath inside an ultrasonic cleaner. This procedure removes grease and other oils from the sample. After the cleaning, the samples have been blow-dried with CO₂ and mounted on a sample plate (made of molybdenum) with an "ear" on one side to allow transportation in situ with a transfer rod. A pocket, to place the sample, and a hole, to allow heating the sample directly by electron bombardment, are drilled into the sample plate. Figure 21 shows a schematic of a sample mounted on a sample plate by spot-welding tantalum clips across the sample to the sample plate. The mounted samples are introduced to the UHV system via the load lock. Once the sample is in UHV, its surface is usually cleaned by argon ion bombardment. Argon is ionized by a hot cathode and accelerated by a high voltage. The ions with energies of around 1 keV hit the surface atoms and start a scattering cascade.

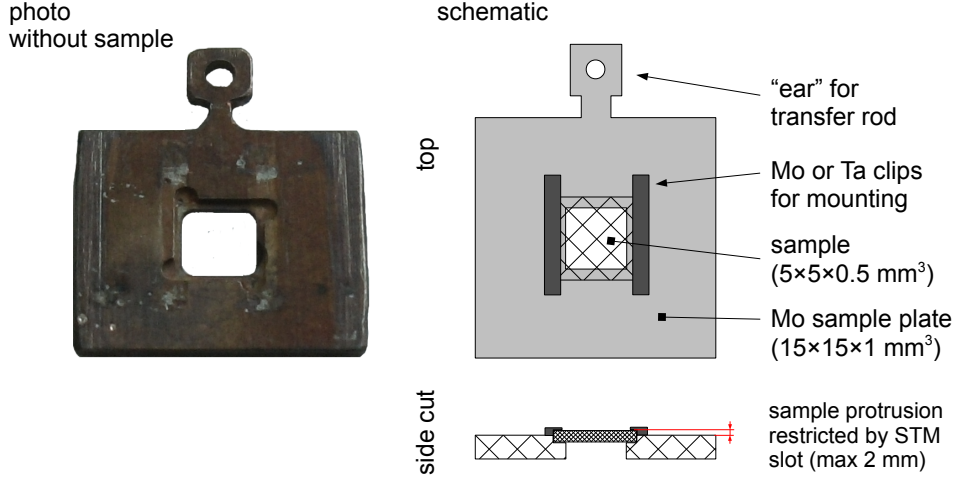


FIGURE 21: Photo and schematic of an Omicron Nanotechnology sample plate adapted to our experiment. The "ear" is for transportation in situ, i.e., within the UHV chambers. The pocket and the hole allow electron-bombardment heating. The sample is mounted with molybdenum or tantalum clips spot-welded onto the sample plate.

With inclined incidence this typically leads to one sputtered-away atom per incident ion (surface atoms as well as impurity atoms), i.e., a sputtering yield of one [38]. Parameters for sputtering and annealing are shown in table 5. The ion current incident onto the sample plate (with an inclination angle of around 45°), which is an indicator of the sputtering dose, was measured as the drain current to the manipulator and was typically in the range of $5-9 \mu\text{A}$. The sputtering parameters can be translated into the total number of argon ions hitting the sample. The ion source used throughout the experiments is a type IQE 11/35 from SPECS GmbH. The specifications report states a Gaussian profile for the beam and a FWHM of around 5.8 mm for a source-sample distance of 50 mm and for ion energies of 1 keV. The ion flux can be estimated to be in the order of $8.5 \times 10^{13} \frac{\text{Ar}^+}{\text{cm}^2 \text{sec}}$. Therefore the total number of ions hitting the sample, with the ion source and sputtering parameters listed above, can be estimated to be in the range of $6-20 \times 10^{15}$ argon ions.

The samples were heated by electron bombardment. A hot cathode (current of around 1.5 A) provides electrons, which get accelerated towards the sample. This typically leads to an emission current of around 13-14 mA, which heats the sample to temperatures well above $850-950^\circ\text{C}$. The temperature was measured with a pyrometer from Micron Instrument Co. Inc.

Sputtering		
p_{Ar} [mbar]	E_{Ar^+} [keV]	time [min]
$2 - 5 \times 10^{-6}$	0.6 - 1	5 - 15
Ion flux estimated: $8.5 \times 10^{13} \frac{\text{Ar}^+}{\text{cm}^2 \text{sec}}$ Argon ions hitting the sample: $6 - 20 \times 10^{15}$		

Annealing		
p_{O_2} [mbar]	T [°C]	time [min]
UHV or $0.5 - 5 \times 10^{-6}$	850 - 950	>40

TABLE 5: Parameters for sputtering and annealing used throughout the experiments.

of type MI-GA 140. The emissivity throughout the measurements was set to 100%. Even though different studies use slightly lower emissivities for the pyrometer, the apparent glowing-color when heating the samples to a pyrometer reading of $\sim 850^\circ\text{C}$ was familiar to Zhiming Wang, the present author’s supervisor, indicating that the temperature reading was correct.

Heating the sample to high temperatures for a rather long time (around 40 min) makes the surface atomically flat. Several of these sputtering and annealing cycles are repeated to obtain a clean and flat surface. For oxide samples, the annealing is usually carried out in an oxygen environment, since annealing in UHV would most likely reduce the sample.

For depositing material onto the surface, several evaporators are mounted on the bottom of the preparation chamber. Strontium was deposited by a CreaTec Fischer & Co. GmbH effusion cell (type LTC), i.e., strontium metal is placed in a crucible and the crucible is heated to around 420°C . Since strontium is chemically reactive and tends to form strontium oxide, e.g., during annealing the sample in oxygen atmosphere, the strontium in the crucible is degassed to 480°C for 15 min before each deposition. Titanium is evaporated using an electron beam evaporator (type EFM) from Omicron Nanotechnology, i.e., electrons from a hot filament are accelerated towards a titanium rod, which is on positive high voltage. This evaporator also provides a feedback for the flux controller by measuring the titanium ion current at its opening. The deposition rate can be measured by a Quartz Crystal Microbalance (QCM). The QCM measures the mass of the material deposited onto it by measuring the change in the mass-dependent resonance frequency of the quartz crystal. The resonance frequency is temperature

dependent and therefore micro balances usually get water-cooled in order to keep the temperature stable. The temperature dependency of the resonance frequency is also following a polynomial of third order. In the present work, the QCM showed to have the maximum of this function at around 90° C. Operating the QCM at this temperature assures minimal variations of the resonance frequency upon variation of the temperature. Depending on the density of the material to be deposited ($\rho_{Sr} = 2.6 \frac{g}{cm^3}$, $\rho_{Ti} = 4.5 \frac{g}{cm^3}$), which is set in the QCM electronics, the controller shows the thickness of the film according to the mass deposited. While the reading of the QCM controller is not an absolute measure of the real flux, it can be used to set the flux relatively to the same value each time. By knowledge of the flux of the evaporators, material can be deposited in precise quantities onto the sample surface. To ensure reordering of the surface layer with the material deposited, samples are usually annealed after deposition.

4 The SrTiO₃(110) Surface

Along $\langle 110 \rangle$ directions, SrTiO₃ is built up of alternating charged layers of SrTiO⁴⁺ and O₂⁴⁻. Because the alternating layers exhibit a net charge of opposite sign, this surface is a polar surface, see figure 1. If the surface were not to be reconstructed electronically or structurally this stacking would lead to a macroscopic dipole perpendicular to the surface [55]. Of course, this situation is energetically very unfavorable. Therefore this surface inherently tends to reconstruct.

Santander-Syro et al. performed angle-resolved photoemission spectroscopy (ARPES) on vacuum-fractured SrTiO₃(001) surfaces [10] and found that a metallic state exists on these surfaces showing an energy-momentum dispersion of free electrons and a quantization of these states, which indicates confinement in one direction. This so-called 2D electron gas (2DEG) on SrTiO₃ surfaces attracts great interest recently since it is a promising feature on the way to oxide-based electronics. They concluded that oxygen vacancies provide the electrons forming this 2DEG. We also study the properties of states inside the forbidden band gap on the SrTiO₃(110) surface by high-resolution ultraviolet photoemission spectroscopy (UPS). We prove that these in-gap states come from oxygen vacancies produced by prolonged exposure to synchrotron light. Since oxygen vacancies are chemically highly reactive, they are not a good and stable choice of producing the 2DEG.

The SrTiO₃(110) (4×1) reconstruction consists of ordered rows along the $[1\bar{1}0]$ direction. Single strontium adatoms sit on top of these rows. Since strontium shows an electronic configuration of [Kr] 5s², it most likely gives away two electrons, i.e., the surface can be doped with electrons by adsorbing strontium. Therefore we study the thermodynamic stability of strontium adatoms on the (4×1) reconstructed SrTiO₃(110) surface.

A structure model of the (4×1) reconstruction has been proposed by Marks et al. [56] and refined by Li et al. [57]. It consists of TiO₄ tetrahedra forming a network of rings on top of a SrTiO plane of the (110) surface. Since titanium is coordinated octahedrally in the bulk and tetrahedrally in the surface layer, we were able to find a signature of the tetrahedral coordination in the XAS spectrum in a surface sensitive mode.

4.1 UPS on SrTiO₃(110) (4×1)

At the MAXLab synchrotron facility, we performed UPS (photon energies in the range of $h\nu = 45\text{-}130\text{ eV}$) on the (4×1) reconstructed surface. Investigation of the valence band and the band gap region of a semiconducting material is of importance, since the valence band actually consists of all the

electrons contributing to features like heat capacity and thermal and electric conductance. Furthermore states within the band gap region are of great interest because these states help the valence band electrons to overcome the band gap stepwise and therefore also enhance the conductivity or support processes taking place on the surface, e.g., photolysis with visible light [7].

We confirmed the reconstruction with LEED. Figure 22 shows a typical LEED image of a (4×1) reconstructed surface:

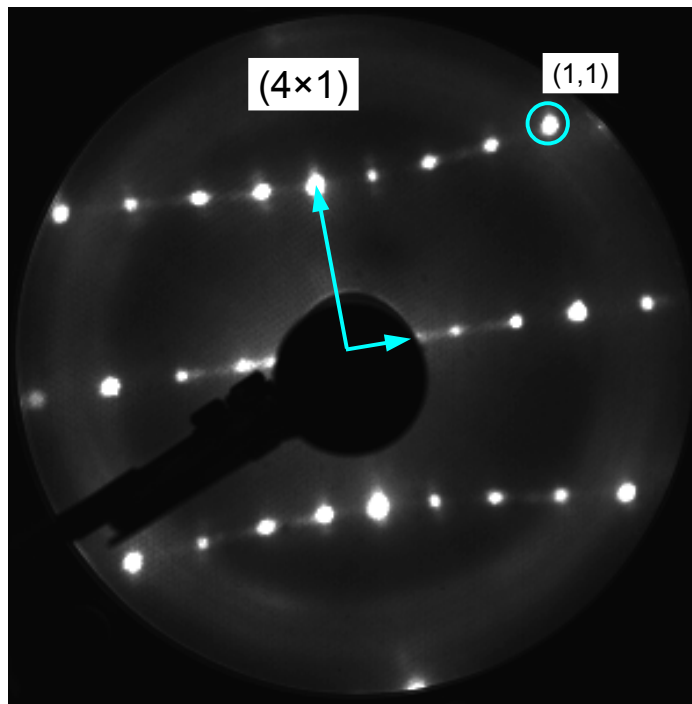


FIGURE 22: Typical LEED image of a (4×1) reconstructed surface. The reciprocal unit cell is indicated with cyan arrows. The $(1,1)$ spot is also indicated. Image taken at 90 eV.

Figure 23 shows a wide range photoelectron spectrum of a $\text{SrTiO}_3(110)$ (4×1) reconstructed surface. The spectrum was taken with an incident photon energy of $h\nu = 1254$ eV. The core level peaks are very sharp and distinguishable and the region with low binding energy is highlighted with a red square. At higher magnifications, also the niobium 3d peak can be distinguished from the background. A photoelectron spectrum ($h\nu = 130$ eV) of the low binding-energy region is shown in figure 24. The uppermost core-levels can be seen as well as the valence band. The valence band comes from the energetically highest occupied states. In the case of STO, these are mainly the oxygen 2p states [14].

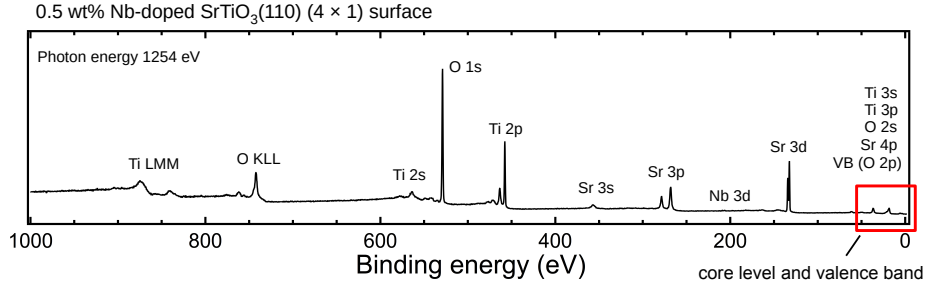


FIGURE 23: High resolution wide range XPS spectrum of a $\text{SrTiO}_3(110) (4 \times 1)$ reconstructed surface. The photon energy was set to the magnesium K_α energy of $h\nu = 1254 \text{ eV}$. The spectrum mainly consists of bulk STO information.

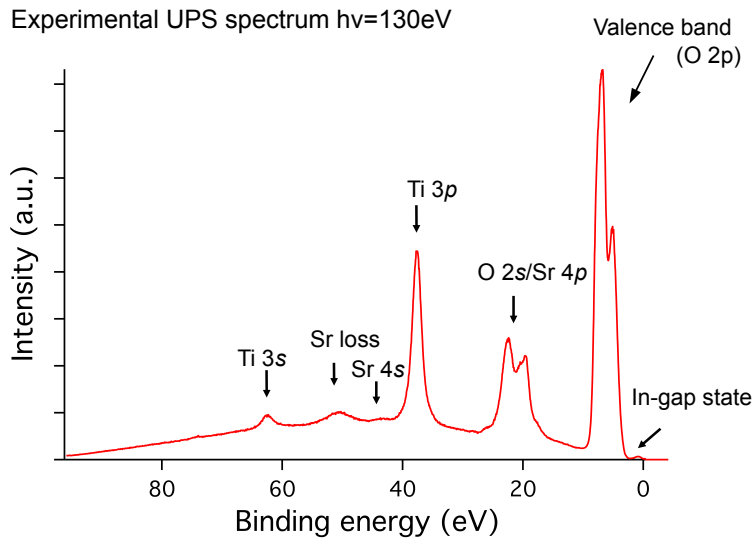
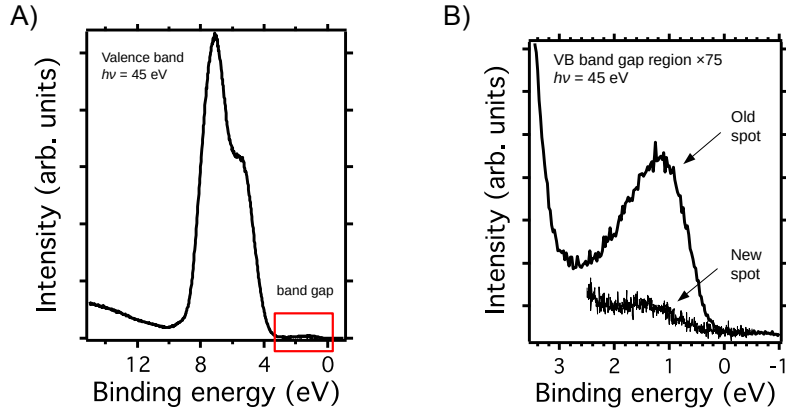


FIGURE 24: High resolution wide range UPS spectrum of a $\text{SrTiO}_3(110) (4 \times 1)$ reconstructed surface. The photon energy was set to $h\nu = 130 \text{ eV}$. The spectrum shows the lowest bound core levels and the valence band. Inside the band gap, an in-gap state is visible.

In the following the focus is laid onto the band gap region. This region is indicated with a red rectangle in figure 25a and shown in detail in figure 25b. We found that if we acquire a band gap region spectrum of a freshly prepared sample, we find the band gap area in the spectrum to be flat with no significant peak in it (in the following called "new spot"). But if we acquire several spectra without moving the sample, i.e., exposing the same spot continuously to synchrotron light, and then take another band gap region spectrum, a peak with significant height appears in the gap region. This peak is in the



A) Valence band spectrum
($h\nu = 45$ eV)

B) Band gap region and in-gap state

FIGURE 25: UPS spectra of the $\text{SrTiO}_3(110)$ (4×1) reconstructed surface: A) Valence band spectrum at $h\nu = 45$ eV. B) Band gap region and in-gap state after exposure to intense synchrotron light (old spot) and after moving to a new area on the sample (new spot).

following called "in-gap state". Aiura et al. already found in their work that this state can be related to the creation of oxygen vacancies [58]. Knotek and Feibelman explain the creation of oxygen vacancies on the surface of TiO_2 , in terms of an inter-atomic Auger process [59]: Incident radiation creates a titanium 3p core-hole. This core hole can be filled via an Auger process. Since the Ti 3p is the highest occupied orbital in titanium, the Auger process requires electrons from other atoms. In the case of TiO_2 the electrons come from the oxygen 2p state. After the inter-atomic Auger process, the oxygen ion (O^{2-}) has lost two electrons and, as a neutral atom, it is easily desorbed. For SrTiO_3 , this electronic picture is quite similar and the creation of oxygen vacancies due to synchrotron radiation most likely follows this process.

We set up an experiment regarding this issue. Figure 26 shows the spectra of this experiment: We recorded a spectrum of a freshly placed sample and observed no state within the gap region (black line). We then created the in-gap state by exposing our sample for some time to intense synchrotron light. After we recorded the spectrum showing the in-gap state (red line) we dosed three Langmuir of oxygen in situ and recorded another spectrum. The spectrum after oxygen dosage (blue line) shows a big decrease of the in-gap state. Therefore the in-gap state is most likely due to the creation of oxygen vacancies.

UPS of band gap region $h\nu=45\text{eV}$

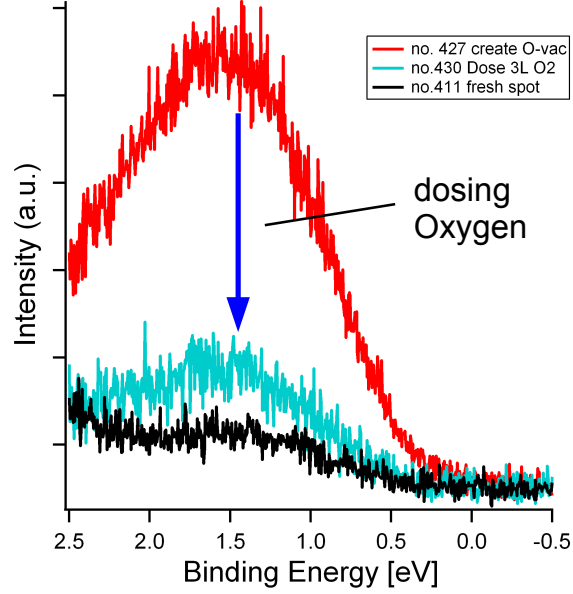


FIGURE 26: UPS Spectrum of band gap region: The spectrum shows a clean surface (black) and a surface after prolonged exposure to synchrotron light (red). If oxygen is dosed onto this surface, the in-gap state decreases dramatically. This indicates that the in-gap state comes from oxygen vacancies.

4.2 Sr Adatoms on the $\text{SrTiO}_3(110) (4\times 1)$ Reconstructed Surface

Figure 27 shows a small-scale STM image of a (4×1) reconstructed surface. The reconstructed rows run along the $[1\bar{1}0]$ direction and the surface shows a periodicity of $(4\times a_{\text{STO}})$ in $[001]$ direction and $(1\times\sqrt{2} a_{\text{STO}})$ in $[1\bar{1}0]$ direction. Therefore this reconstruction is called (4×1) . Bright spots appearing within the rows were found to be strontium adatoms [34]. Figure 28 shows an STM image of an as-prepared $\text{SrTiO}_3(110)$ surface by sputtering and annealing with typical parameters for SrTiO_3 surfaces (see table 5). The surface consists of (4×1) reconstructed rows running along the $[1\bar{1}0]$ direction and areas, which are more blurry in appearance. The blurry feature was found by Wang et al. to exhibit a (2×4) periodicity [34].

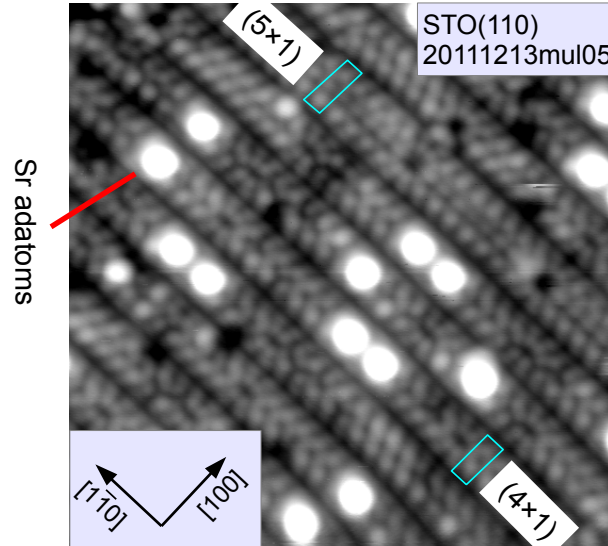


FIGURE 27: Small scale STM image of a (4×1) reconstructed $\text{SrTiO}_3(110)$ surface. One row showing a (5×1) reconstruction is also visible. The bright dots are found to be strontium adatoms [34]. The image ($15\times 15\text{ nm}^2$) was scanned by Zhiming Wang with $+2.3\text{ V}$ and 0.25 nA .

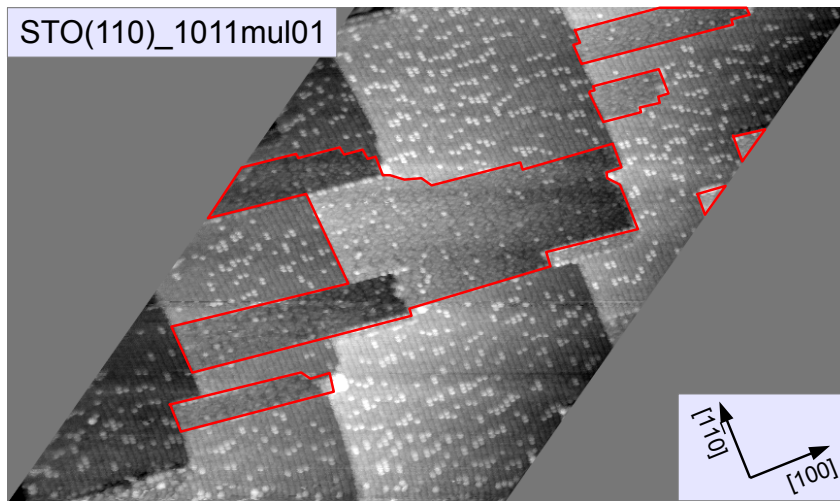


FIGURE 28: STM image of an as-prepared $\text{SrTiO}_3(110)$ surface. The surface shows reconstructed rows along the $[\bar{1}10]$ direction, which is called the (4×1) reconstruction. The reconstructions inside the red lines are found to have a (2×4) periodicity [34]. The image ($150\times 150\text{ nm}^2$) was scanned with $+2.4\text{ V}$ and 0.5 nA . Due to problems with the scanner (see ch. 3.2.3), the original image is heavily distorted. It is shown here in undistorted form.

The surface in figure 28 can easily be transformed into a single terminated surface just showing the (4×1) reconstruction. This can be done by using the surface phase diagram (figure 29) developed by Wang et al. [34]: The STM image reveals roughly how much of the surface shows the (2×4) reconstruction. In the image above, the percentage of (2×4) reconstruction is estimated using image processing to be around 25%. Applying this value on the amount of strontium necessary to fully change from (2×4) to (4×1) , i.e., 0.75 ML (value from phase diagram), we find the right amount of strontium to be deposited. In this case we had to deposit $0.75 \text{ ML} \cdot 0.25 = 0.19 \text{ ML}$, which corresponds to an amount of 1.9 \AA related to the QCM reading.

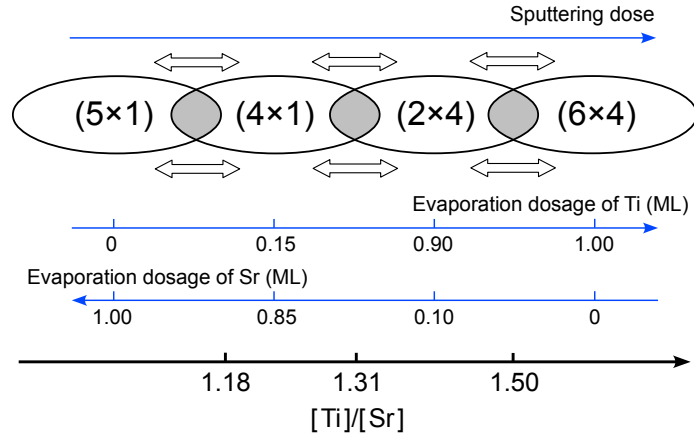


FIGURE 29: The phase diagram of the $\text{SrTiO}_3(110)$ surface depending on the sputtering dose or the Ti or Sr metal deposition (in monolayers, ML). Reconstructions are labeled as $(n\times m)$, meaning $(n \cdot a_{\text{STO}(001)} \times m \cdot a_{\text{STO}(110)})$. Image taken from reference [34].

The surface after depositing an appropriate amount of strontium and annealing in 10^{-6} mbar oxygen is shown in figure 30. The surface structure fully changed into the (4×1) reconstruction. We used this surface as the template for the growth of strontium adatoms.

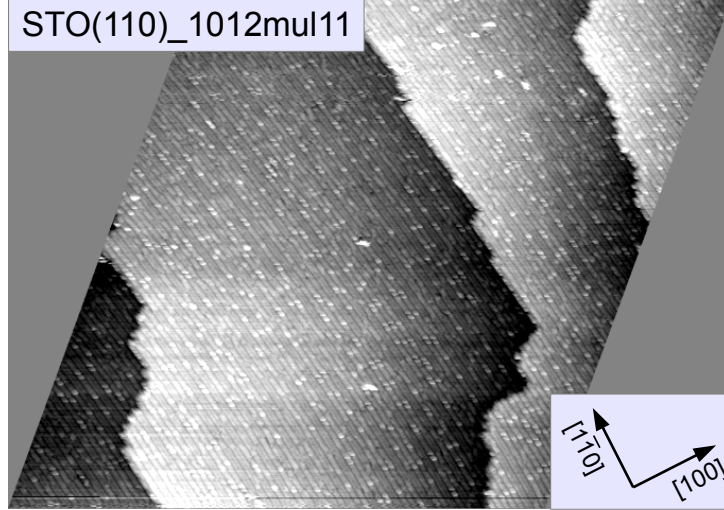
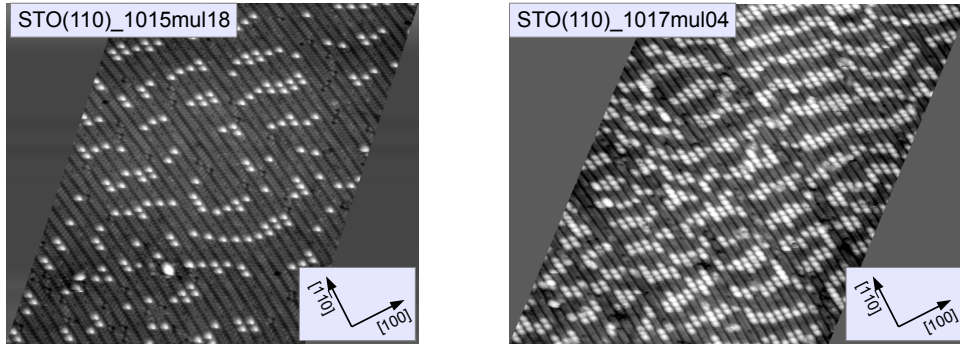


FIGURE 30: After evaporating the appropriate amount of strontium onto the surface from figure 28 and annealing in 10^{-6} mbar O_2 , the surface structure fully changed into a (4×1) single terminated surface.

4.3 Thermal Stability of the Sr Adatoms

We studied the deposition of single strontium adatoms on the (4×1) reconstruction and investigated the thermal stability of these. From figure 27 it can be seen that strontium adsorbs on this surface as single adatoms. Since strontium has two electrons outside of filled shells, each single adatom dopes the surface with two electrons. This can lead to metallic states inside the band gap and has become of great interest recently. To conduct experiments related to this topic, the thermodynamic stability of the strontium adatoms has to be studied. Figure 31 shows two STM images of a (4×1) reconstructed surface before and after depositing an amount of strontium corresponding to a QCM reading of 1 \AA . The surface was annealed to 340° C to assure reordering of the adatoms. After all depositions and for the temperature-dependent experiments, the sample has always been annealed in an oxygen atmosphere in the order of 10^{-6} mbar.

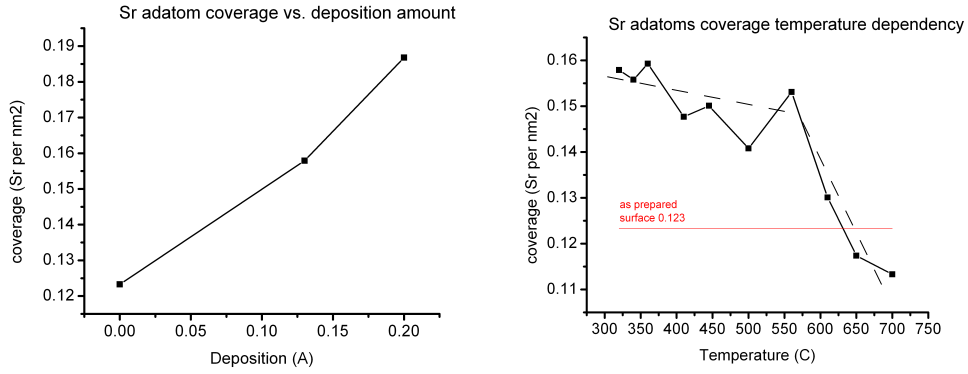


A) $50 \times 50 \text{ nm}^2$, +2.7 V, 0.15 nA

B) $70 \times 70 \text{ nm}^2$, +1.5 V, 0.34 nA

FIGURE 31: A) STM image of a typical single terminated (4×1) surface. B) STM image of the same surface after deposition of strontium and annealing to around 340°C in 10^{-6} mbar O_2 .

The adatoms do not form clusters and there is some ordering visible. The nearest and also most commonly observed distance between two adatoms is found to be two times the unit cell in $[1\bar{1}0]$ direction. With image processing we analyzed a series of STM images after depositing a certain amount of strontium and annealing to various temperatures. Figure 32a shows the relation of the strontium deposition measured with the QCM to the density of Sr-adatoms after annealing to 340°C . The graph shows more or less a straight line, which means that we did not lose any adatoms during annealing to 340°C and that we did not reach the saturation coverage. The density of Sr-adatoms was determined by counting the bright spots in the STM images by use of image-processing. These values were divided by the size of the STM image. The mean value of the density after analyzing at least three STM images was taken. Figure 32b compares the analyzed density of strontium adatoms after annealing the sample to different temperatures. It can be seen that the density of adatoms decreases slowly with temperature until at around 600°C the density shows a sudden drop. According to the phase diagram (figure 29), deposition of strontium and annealing in oxygen transforms the (4×1) into the (5×1) reconstruction. This can also be seen in STM. Figure 33 shows a (4×1) reconstructed surface with a small amount of (5×1) reconstruction (highlighted in cyan).



A) Sr adatom density vs. Sr deposition B) Sr adatom density vs. annealing Temp.

FIGURE 32: A) Analyzed strontium adatom density upon strontium deposition and annealing to 340° C in 10⁻⁶ mbar O₂. B) Comparison of analyzed Sr adatom density after annealing the sample to different temperatures. The starting coverage was 0.16. The density shows a drop at around 600° C.

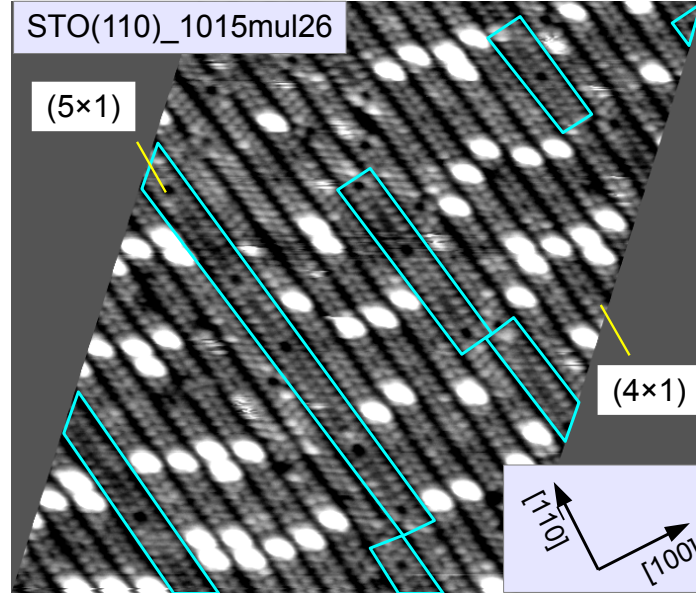


FIGURE 33: STM image (30 × 30 nm²) of a (4×1) reconstructed surface with increased amount of Sr adatoms after annealing to T>600° C. A (5×1) reconstruction formed because of the deposited Sr (compare figure 29). The image was measured with +2.1 V and 0.35 nA.

4.4 XAS on SrTiO₃(110) (4×1)

The structure model of the (4×1) reconstruction consists of corner sharing TiO₄ tetrahedra forming a network of six- and ten-membered rings on the surface [56]. The six-membered rings protrude out of the surface and appear as bright rows in STM. The ten-membered rings build the dark trenches in STM. Figure 34 shows a top and a side view of the structure model. The side view shows that the tetrahedrally coordinated titanium in the (4×1) layer sits directly on top of a titanium-strontium-oxygen plane with octahedrally coordinated titanium. Since XAS is a technique sensitive to the chemical coordination of an atom, we were able to find a proof for the tetrahedrally coordinated titanium in the SrTiO₃(110) (4×1) reconstructed surface.

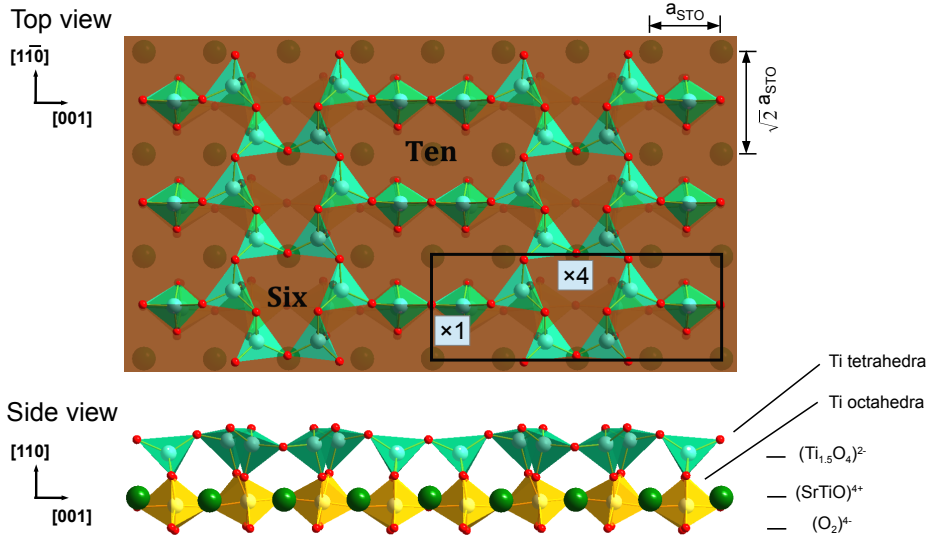


FIGURE 34: Top and side view of the (4×1) structure model [56]: It consists of a network of six- and ten-membered rings. The (4×1) reconstructed rows run along the $[1\bar{1}0]$ direction. The model shows that TiO₄ tetrahedra of the surface sit on top of the TiO₆ octahedra from the bulk.

We performed XAS in two different modes (see section 3.3), in TEY mode (bulk sensitive) and in AEY mode (surface sensitive). Figure 35 shows the experimental XAS spectrum of the Ti⁴⁺ L_{2,3} absorption edge in TEY and AEY mode. The surface sensitive AEY spectrum shows an additional peak. If we simulate an XAS spectrum of a Ti⁴⁺ L_{2,3} absorption edge for a tetrahedral and an octahedral coordination of the titanium, we find that the additional peak in the AEY spectrum corresponds to a tetrahedrally coordinated titanium. This is in perfect agreement with the structure model

proposed. Figure 36 shows the simulated spectrum. The spectrum was simulated using the software CTM4XAS by de Groot and Stavitski [60]. It is used for XAS spectral shape analysis.

Experimental Ti^{4+} $L_{2,3}$ XAS spectrum

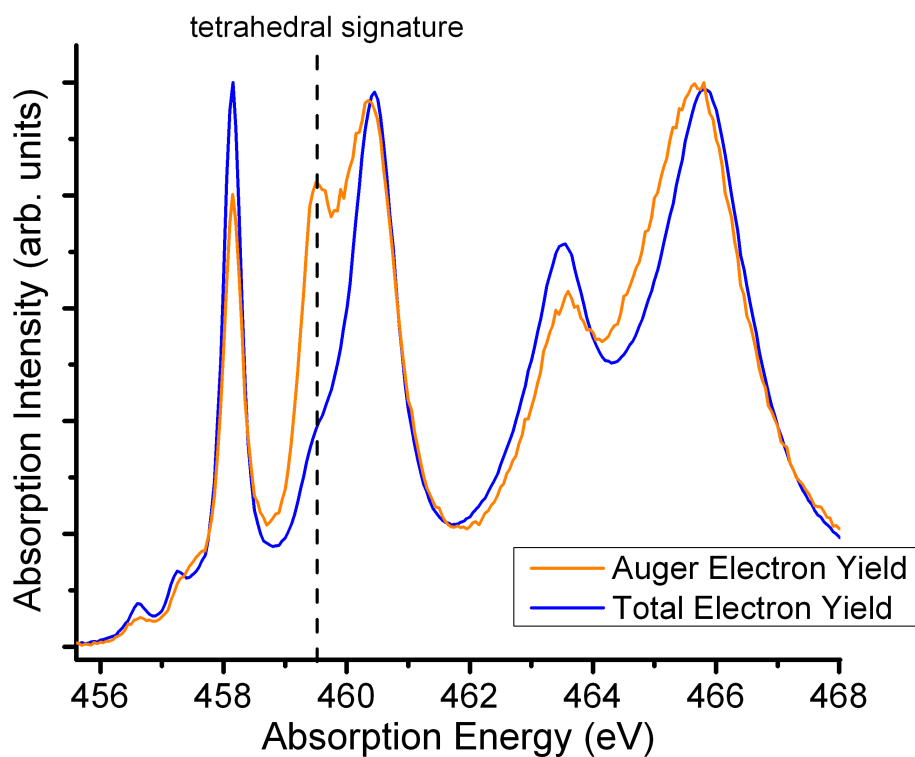


FIGURE 35: XAS spectra of the Ti^{4+} $L_{2,3}$ absorption edge in TEY and AEY mode. In the surface sensitive AEY spectrum, an additional peak arises.

Simulated Ti^{4+} $L_{2,3}$ XAS spectrum

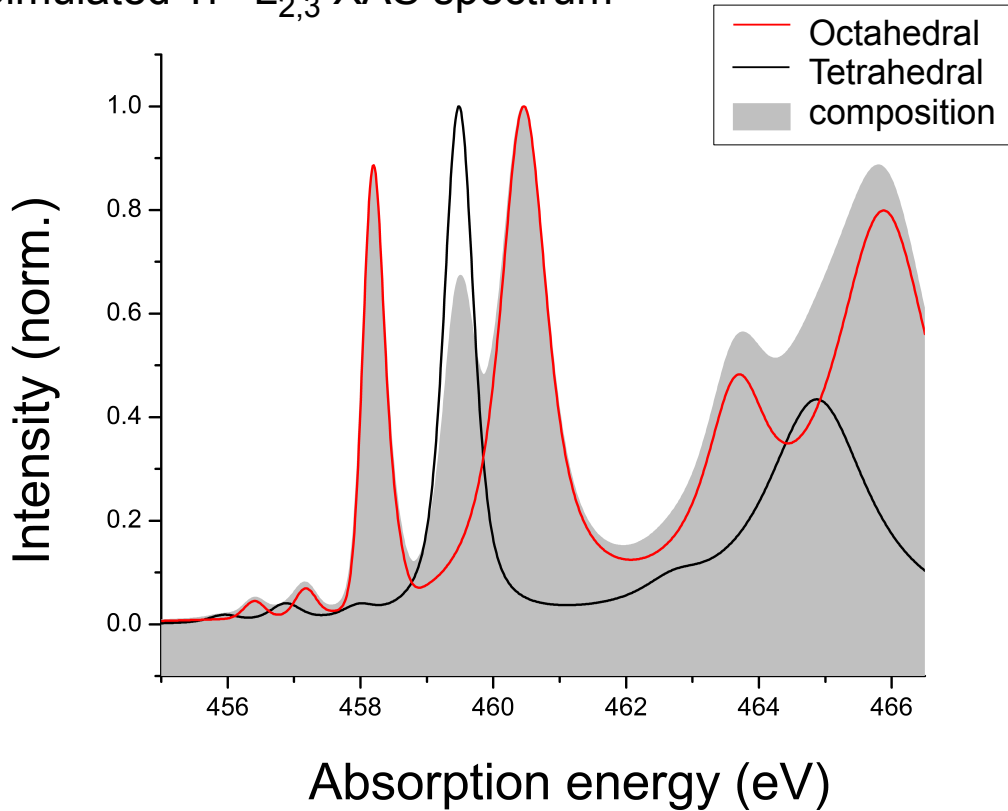


FIGURE 36: Simulated spectra of a Ti^{4+} $L_{2,3}$ absorption edge for octahedrally coordinated and tetrahedrally coordinated titanium. A composition of both, the tetrahedrally and octahedrally coordinated titanium is in excellent agreement with the experimental spectrum of figure 35.

The (4×1) structure is part of a homologous series of reconstructions on the $\text{SrTiO}_3(110)$ surface. By adding additional TiO_4 tetrahedra into the six-membered ring of the (4×1) structure, the (4×1) structure can be transformed into the (5×1) and additional TiO_4 tetrahedra even transforms the (5×1) structure into the (6×1) structure. The ten-membered rings stay the same for all structures [57]. Figure 37 shows the structure model for the $(n \times 1)$ structure series.

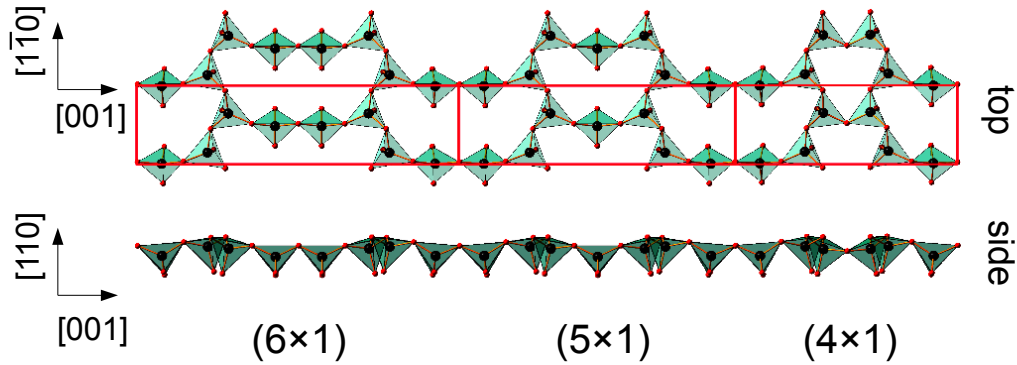


FIGURE 37: Structure model for the $(n \times 1)$ reconstructions of the $\text{SrTiO}_3(110)$ surface. The model consists of corner sharing TiO_4 tetrahedra forming a network of rings. It was proposed by Marks et al. [56] and refined by Li et al. [57].

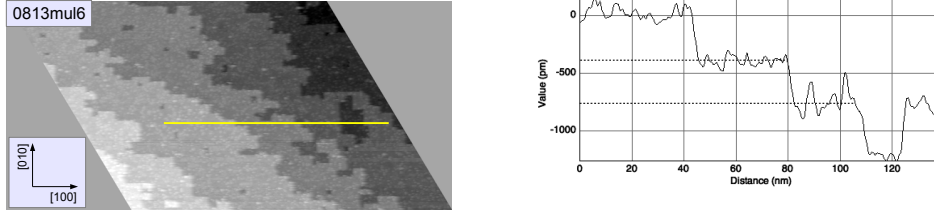
The series of $(n \times 1)$ reconstructions is also part of the surface phase diagram developed by Wang et al. [34]. They found that a series of reconstructions on the $\text{SrTiO}_3(110)$ surface can be controlled and changed reversibly into each other by controlling the surface stoichiometry. Figure 29 shows the stoichiometry driven phase diagram of $\text{SrTiO}_3(110)$ reconstructions. Depositing a certain amount of strontium or titanium onto the surface and annealing in oxygen changes the structure reversibly. The driving force is a control of the surface stoichiometry. It can be seen in figure 37 that the amount of titanium per surface unit cell decreases from (4×1) to (6×1) .

5 The SrTiO₃(001) Surface

Interesting effects are taking place on SrTiO₃ surfaces, e.g., photolysis and 2DEG. However, all of these effects are restricted to atomically well defined surfaces and therefore one has to be able to produce mono-phased surfaces exhibiting the structure of choice. While a literature review shows that SrTiO₃ surfaces show a huge variety of reconstructions, also the preparation procedures require a precise control of the sputtering and annealing parameters (Ar⁺ dosage and T_{ann.} and p_{O₂ ann.}). This fact shows the elegance of the approach of Wang et al.. They showed that a series of reconstructions on the SrTiO₃(110) surface can be tuned into each other reversibly by adjusting the strontium or titanium evaporation dose and annealing in 10⁻⁶ mbar oxygen (see figure 29 from reference [34]). This is the case, because each reconstruction exhibits a different surface stoichiometry and because the stoichiometry is the driving force that changes the reconstructions reversibly into each other. In this work, we found that also on the SrTiO₃(001) surface, a small series of structures, namely the c(4×2), the (2×2) and a (1×1) structure, can be changed into each other reversibly by adjusting the strontium or titanium evaporation dosage and annealing in 10⁻⁶ mbar oxygen. This indicates that also on (001) surface, the structures exhibit a different stoichiometry. Therefore the c(4×2) and the (2×2) reconstructed surfaces have been investigated by XPS and ISS. While the XPS spectra do not reveal any difference in composition, ISS shows that the (2×2) reconstruction is rich in strontium while the c(4×2) reconstruction is rich in titanium. This is in agreement with the preparation procedures and supports the theory that each reconstruction exhibits a different stoichiometry. This is in contradiction to models proposed in the literature, which will be discussed in the end of this chapter.

5.1 SrTiO₃(001) - Deposition of Sr and Ti

The SrTiO₃(001) samples have been repeatedly sputtered and annealed until a sharp LEED pattern occurred. Throughout the experiments, the parameters used for sputtering with Ar⁺ ions and annealing in oxygen are listed in table 5. If the sample was annealed in UHV, it will be mentioned specifically. After Sr or Ti deposition, the time for annealing in oxygen was only around 15 min. Figure 38 shows an STM image of a sample introduced to the UHV system and sputtered and annealed once. Most of the STM images in this chapter are skewed, because of a problem with the STM scanner (see section 3.2.3 "STM Scanner Depolarization and Calibration"). The step edges are ragged and there are still islands and holes on the terraces. This is most



A) $200 \times 130 \text{ nm}^2$, +2.7 V, 0.28 nA

B) Line profile

FIGURE 38: A) STM of once-sputtered and annealed $\text{SrTiO}_3(001)$ sample: The terraces are flat with a size of around 20 nm. The profile along the line B) shows terraces with steps of around 4 \AA height (equal to one unit cell of STO).

probably because the annealing temperature was not sufficiently high. However, the terraces are already flat and from the profile across the terraces, the step height equals one unit cell of SrTiO_3 . This means that either the polishing by the crystal vendor preferentially leaves behind a single terminated surface, or the sputtering preferentially sputters away either strontium or titanium.

LEED of this surface shows a clear pattern (see figure 39). By comparison with a simulated LEED image this structure is associated with a so-called $c(4 \times 2)$ structure. Figure 40 shows a schematic of a TiO_2 terminated surface exhibiting a two-domain $c(4 \times 2)$ reconstruction. The reconstructed sites (indicated in cyan) are placed on oxygen sites, e.g., the reconstruction could stem from ordered O-vacancies. But there are other theories, e.g., one proposing ordered Sr adatoms [25] or one proposing ordered TiO_x -clusters [61, 62]. This will be discussed later. Since the unit cell of a $c(4 \times 2)$ structure is of rectangular shape, two domains (indicated in different colors in figure 39b) co-exist on the surface with a rotation of 90 degrees with respect to each other. Additional sputtering and annealing cycles make the surface atomically flat without islands or pits. Figure 41 shows a large-scale STM image of a $c(4 \times 2)$ surface and a line scan across the terraces to show the step height of a single unit cell ($a_{\text{SrTiO}_3} = 3.905 \text{ \AA}$). The step edges are now much less ragged and the size of the terraces is still in the range of 20 – 30 nm. This surface can also be resolved atomically in STM, which is seen in figure 42a. The fast Fourier transformation (FFT) of the STM image can be used to find the correct parameters for undistortion. In ImageJ, the FFT spots are used to build the reciprocal unit cell. The length and the angle between the vectors building the reciprocal unit cell can be compared with the expected values of a $c(4 \times 2)$ structure. With this input, the program is able to cal-

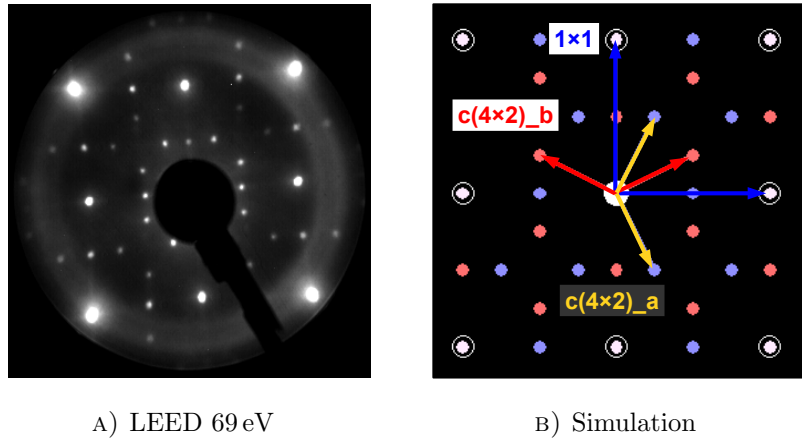


FIGURE 39: Confirmation of a two-domain $c(4\times 2)$ structure by comparing LEED experiment (A) and simulation (B). The contribution of the two domains are indicated in colors.

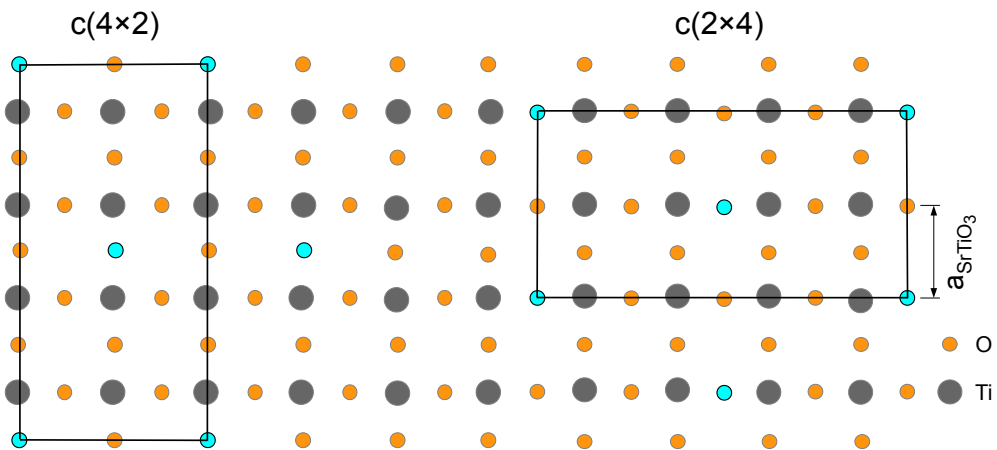
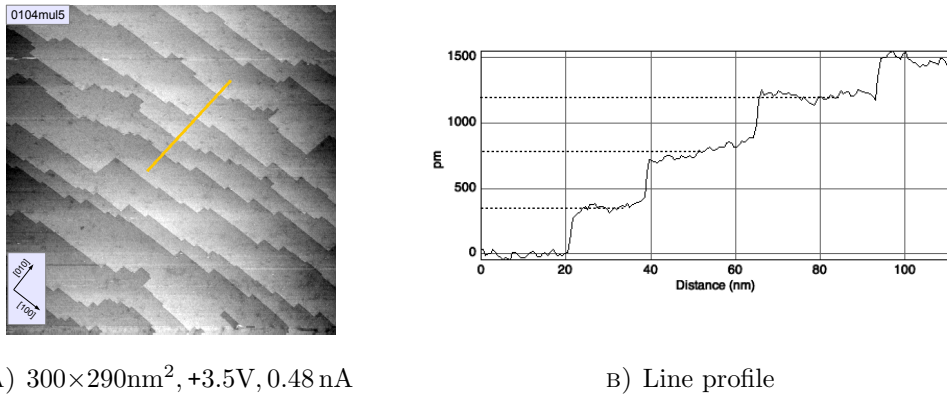


FIGURE 40: Schematic of two domains of a $c(4\times 2)$ structure on a TiO_2 terminated $\text{SrTiO}_3(001)$ surface. The reconstructed site is indicated in cyan.

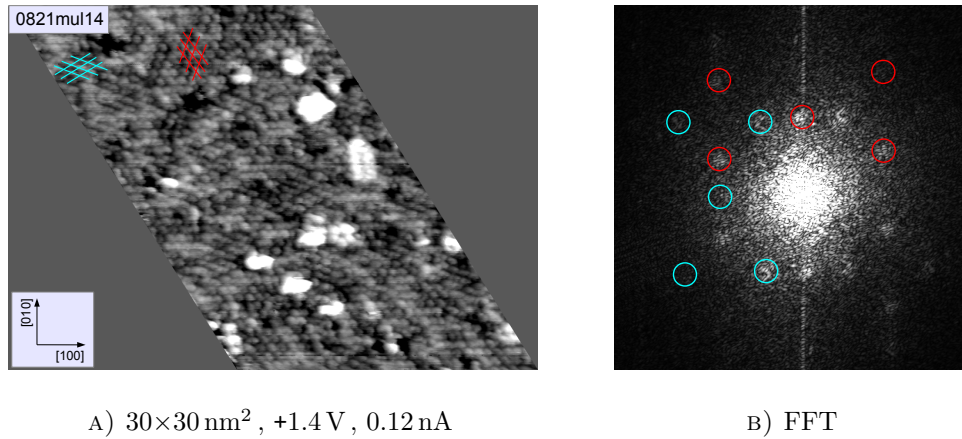
calculate a shear angle and a ratio for both scanning directions to undistort the STM image. Figure 42a shows the undistorted STM image and the two domains, indicated in cyan and red respectively, are correctly rotated by 90° with respect to each other. Figure 42b shows the fast Fourier transformation (FFT) of the undistorted STM image in A). The two domains of the $c(4 \times 2)$ structure are also indicated in red and cyan.



A) $300 \times 290 \text{ nm}^2$, +3.5V, 0.48 nA

B) Line profile

FIGURE 41: A) Large-scale STM image of a surface showing a sharp $c(4 \times 2)$ LEED pattern. The terraces are flat with a size of around 20 nm. The profile along the line B) shows terraces with steps of around 4 \AA height (equal to one unit cell of SrTiO_3).

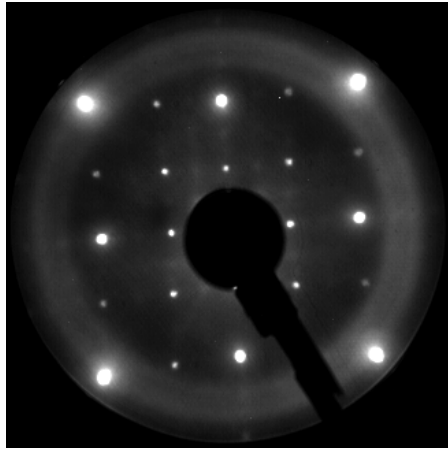


A) $30 \times 30 \text{ nm}^2$, +1.4V, 0.12 nA

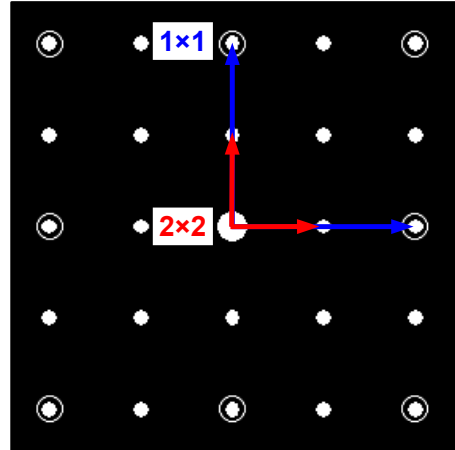
B) FFT

FIGURE 42: A) STM image of a surface showing a sharp $c(4 \times 2)$ pattern. The image had to be undistorted. The two domains are indicated in red and cyan. B) shows the FFT of the image in A). The spots of the two domains of the reciprocal $c(4 \times 2)$ unit cells are visible.

Strontium was evaporated onto this surface. To bring the surface with the material deposited into thermodynamic equilibrium and to also assure a reordering of the surface layer, the sample was annealed in an oxygen atmosphere of $\sim 10^{-6}$ mbar. Because annealing the sample was always applied after deposition or sputtering, the procedures in the following are only written in terms of deposition or sputtering only. Strontium was evaporated onto this surface until a change in the LEED pattern occurred. Strontium evaporation temperatures of 415° C to 450° C lead to a flux, measured with a QCM, in the range of 1 Å in 15 to 60 seconds. After evaporating an amount of strontium corresponding to a reading of 3 Å on the QCM controller, the resulting surface showed a (2×2) symmetry in LEED. Figure 43 shows a comparison of an experimental and a simulated LEED image of this surface. The spots are quite sharp and intense, which is probably related to a uniformity of the structure across the surface. Figure 44 shows a large-scale STM image of this surface with terraces of approximately 20 nm width and with step heights of around 0.4 nm. The step height is of one unit cell, which indicates single termination. The step edges are now wavy, which is different to the c(4×2) surface. This indicates a different building block. It was not possible to image this surface with atomic resolution. The scanning in a small scale (below an image size of 30 × 30 nm²) was not stable. This could be due to local jumps in the conductivity of the surface layer or due to the presence of adsorbates on the surface. In analogy to the surface preparation procedure of Wang et al. for tuning the reconstructions on the SrTiO₃(110) surface in both directions, titanium was deposited onto the (2×2) reconstructed surface. We found that the structure can be changed back into the original c(4×2) reconstruction by evaporating titanium onto this surface and annealing in oxygen. The amount of titanium deposited to switch from a (2×2) to a c(4×2) reconstructed surface was determined by the reading of the QCM controller and was in the range of 0.3-0.4 Å. Figures 46 to 48 show an overview of the deposition procedures applied. They show the SrTiO₃(001) surface structures, determined by LEED, upon evaporation of strontium or titanium onto the surface or by sputtering. Each mark corresponds to one LEED measurement after a deposition procedure or sputtering. The amount of Sr or Ti deposited or the procedure applied, such as sputtering or annealing in O₂ or UHV, is indicated in abbreviations, which are explained in the legend. Deposition of strontium or titanium is indicated with blue or red arrows, respectively. Thick arrows indicate a higher deposition-amount. Figure 45 shows the different experimental LEED patterns observed. The sharp patterns of a c(4×2) and a (2×2) reconstructed surface can be seen in figures 39 and 43, respectively. Faint versions of these patterns are in quality similar to the mixed pattern in figure 45b.

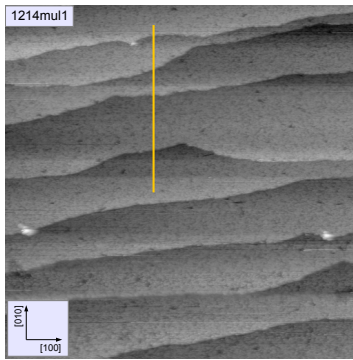


A) Experiment

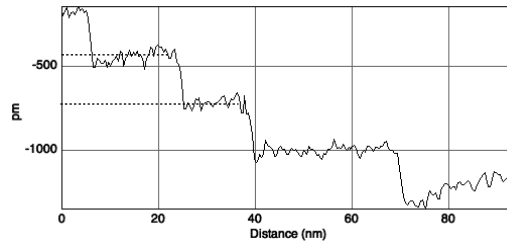


B) Simulation

FIGURE 43: Confirmation of (2×2) structure by comparing experimental and simulated LEED images.



A) $200 \times 200 \text{ nm}^2$, +2.3 V, 0.26 nA



B) Line profile

FIGURE 44: A) STM image of a surface fully changed from $c(4 \times 2)$ into a (2×2) (determined by LEED). The terraces are flat with a size of around 20 nm. B) The profile along the yellow line in (A) shows terraces with steps of around 4 \AA height (equal to one unit cell of SrTiO_3). The background subtraction for the image as shown in A) was different from the one used for obtaining the line profile.

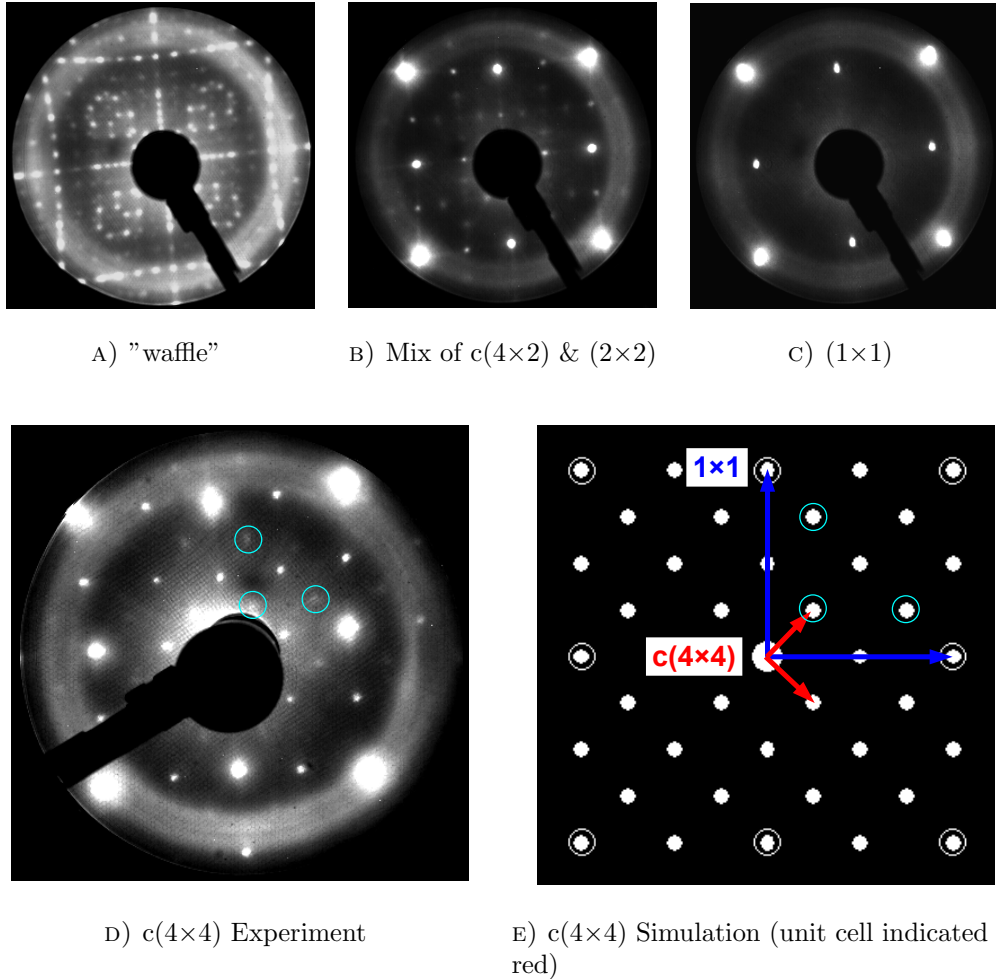


FIGURE 45: LEED patterns occurring after sputtering (A) or deposition of strontium or titanium (B, C). (D) Observation and (E) confirmation of a $c(4 \times 4)$ structure, which forms upon annealing a (2×2) reconstructed surface in UHV. The structure in (A) is called waffle structure according to reference [63].

From the pseudo-phase-diagram (figures 46 to 48) it can be seen that Sr deposition drives the structure to the right (towards (2×2) , and further to (1×1)). Deposition of Ti drives the structure to the left (towards $c(4 \times 2)$). It can also be seen that sputtering acts Ti enriching, which is in good agreement with the work of Wang et al. (compare figure 29). A $c(4 \times 4)$ and a (4×4) structure (confirmed by analyzing STM images) formed upon annealing a (2×2) surface in UHV. The $c(2 \times 2)$ structure formed after depositing additional strontium onto the (1×1) structure.

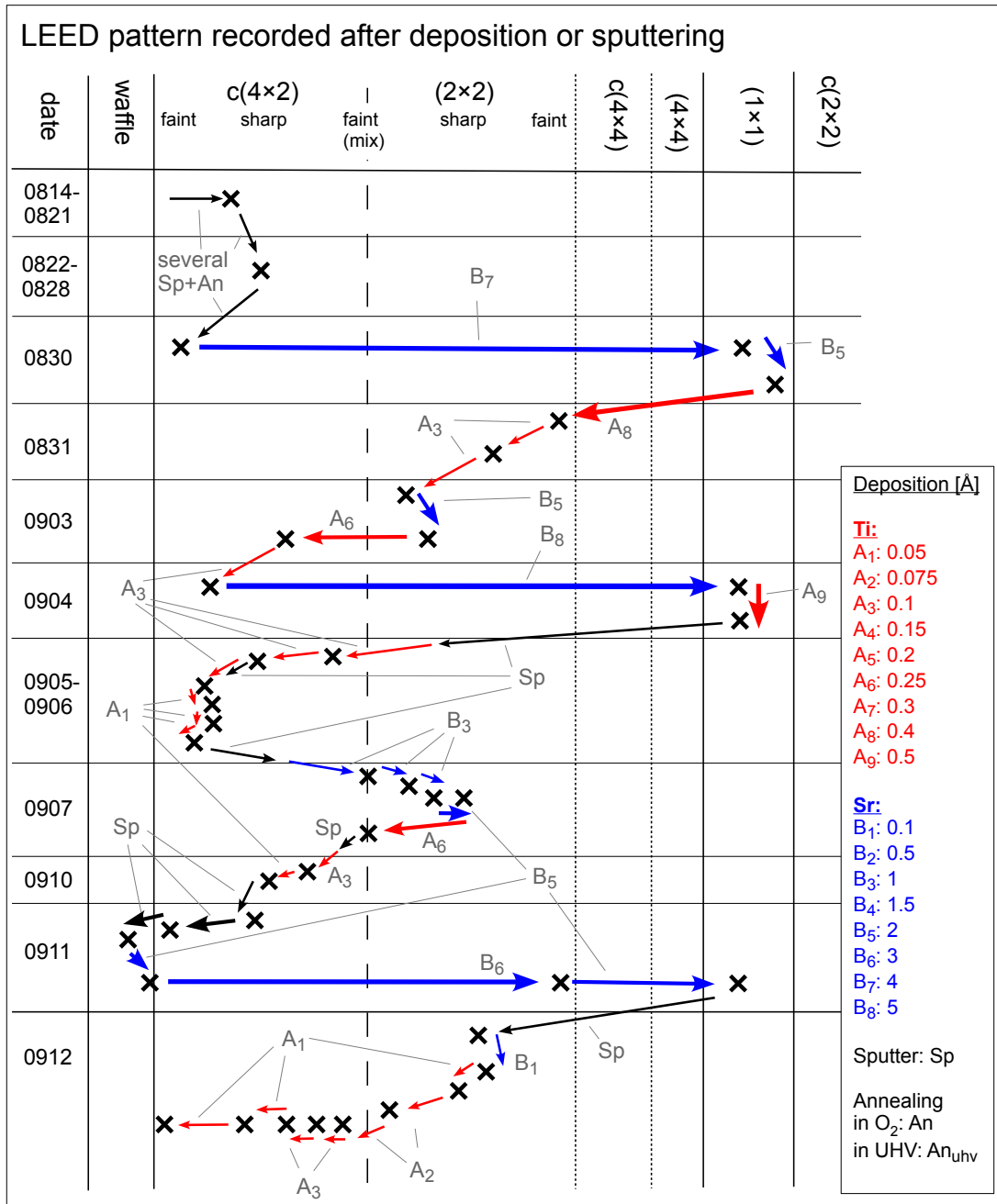


FIGURE 46: Summary (part 1) of LEED pattern determined structures upon deposition of strontium or titanium: Sputtering tends to result in titanium enrichment. Some structures formed upon annealing in UHV. Annealing in oxygen was done after deposition or sputtering.

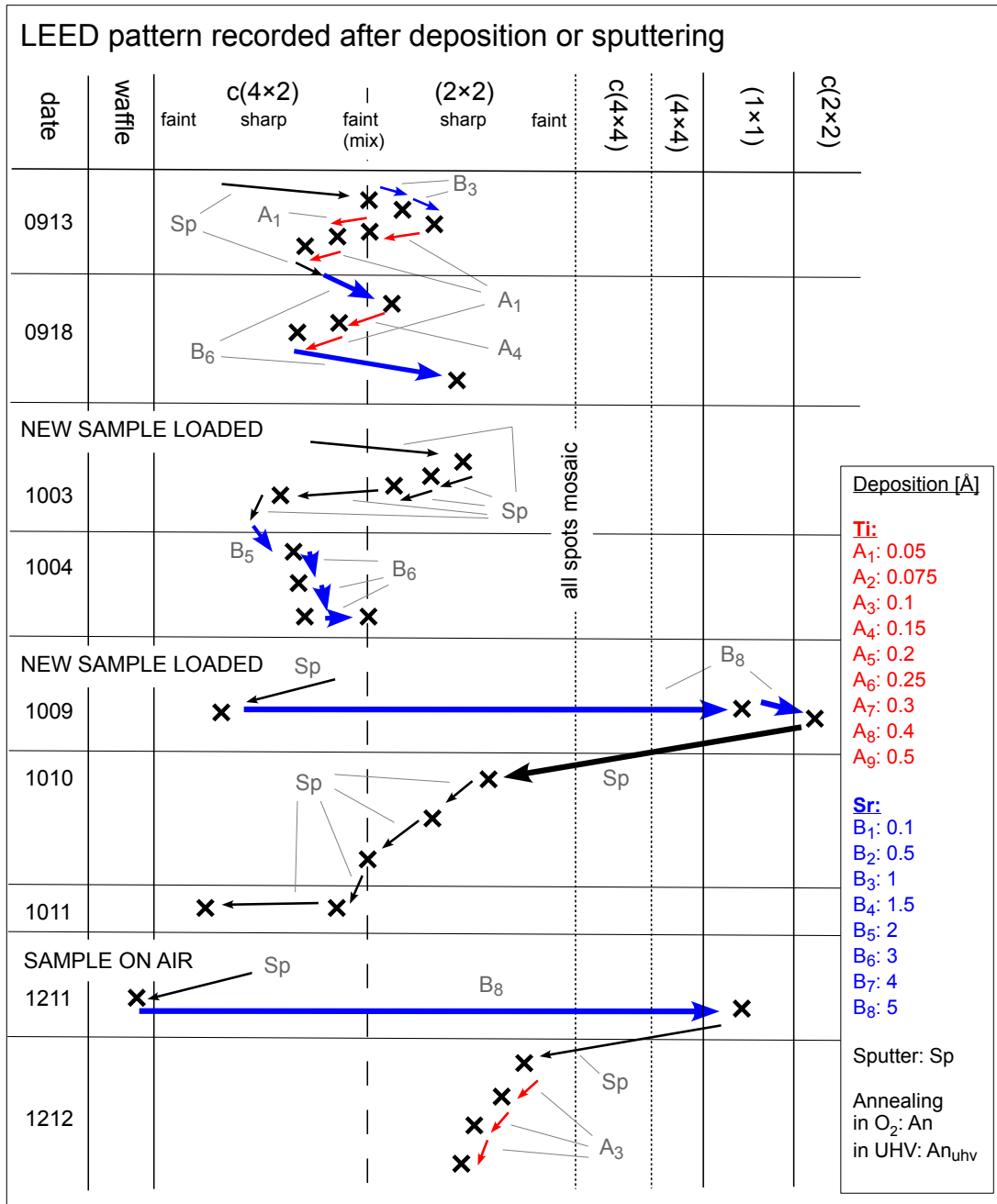


FIGURE 47: Continuation of figure 46.

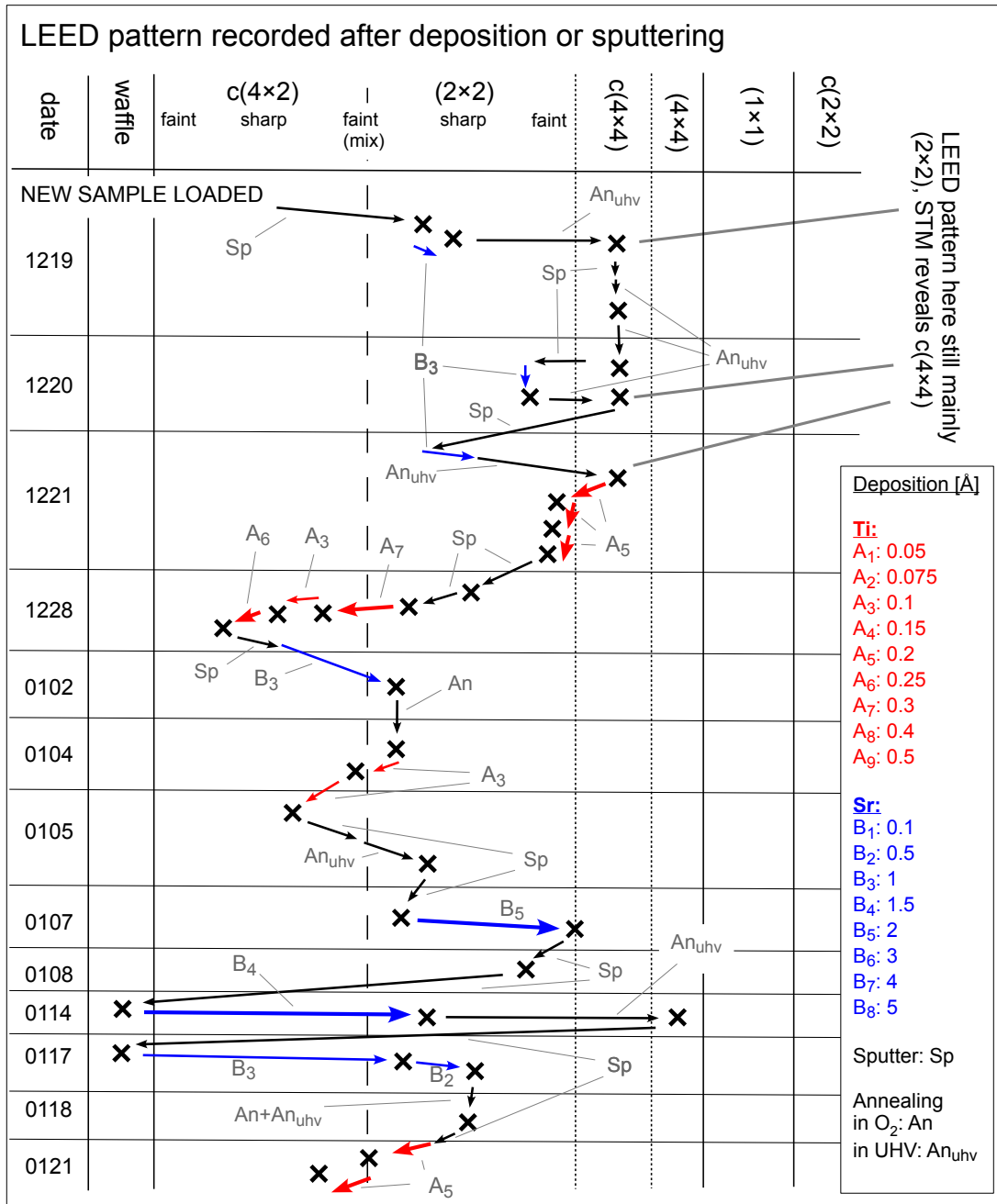


FIGURE 48: Continuation of figure 47.

No atomically resolved images could be obtained from the (2×2) reconstructed surface. A possible reason for this could be a lack of conductivity in regions of the surface layer. Thus, the (2×2) surface was flashed to high temperatures in UHV for 5-10 min. This was assumed to create oxygen vacancies, i.e., to reduce the crystal and the surface layer, and therefore to increase the conductivity. The resulting surface could be scanned with atomic resolution. LEED of this surface still showed mostly a (2×2) structure with some faint spots of a $c(4 \times 4)$ structure (see figure 45d and 45e). Figure 49a shows a terrace that is almost completely covered by a $c(4 \times 4)$ structure. Figure 49b shows a small scale image of this structure. Along the line, the periodicity is measured to be 1.62 nm, which is close to four times the lattice constant of SrTiO_3 ($a_{\text{STO}} = 0.39 \text{ nm}$). Therefore this structure is assumed to be a $c(4 \times 4)$ structure. The process of creating a $c(4 \times 4)$ structure upon annealing the sample in UHV has already been reported by Castell et al. [23]. It should be mentioned that in their study, the surface prior to the UHV annealing showed a (2×1) structure.

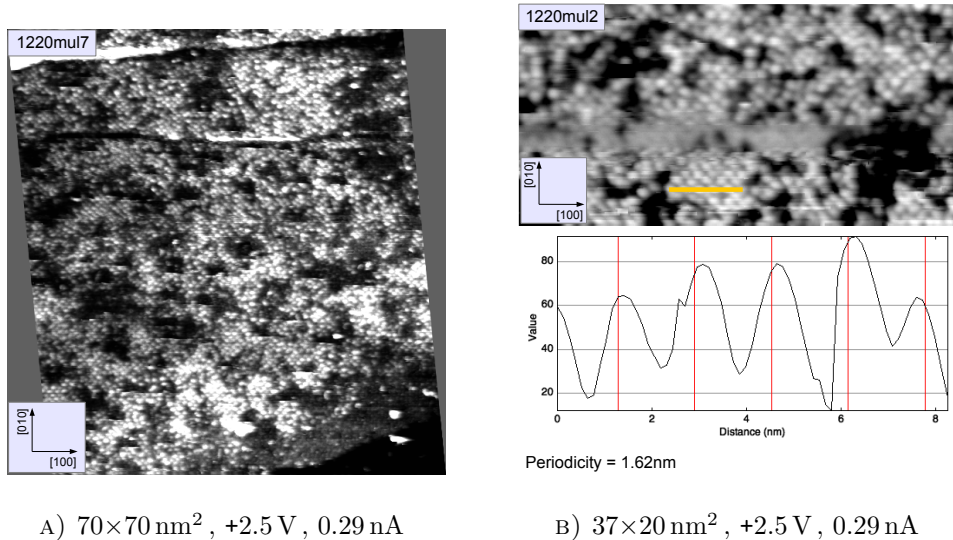
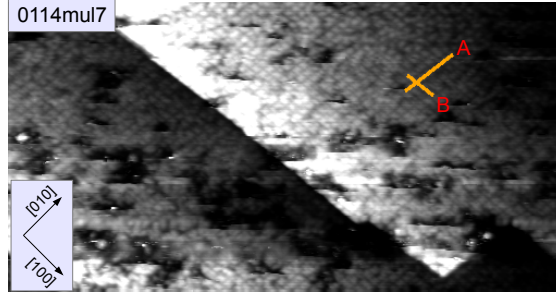
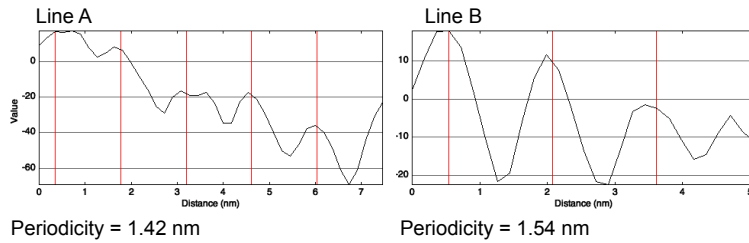


FIGURE 49: A) Medium scale STM image of a $c(4 \times 4)$ reconstructed surface. B) Small scale of $c(4 \times 4)$. The periodicity along the line is measured to be 1.62 nm, which is close to four times the lattice constant of SrTiO_3 .



A) $70 \times 36 \text{ nm}^2$, +3.4 V, 0.36 nA



B) Profiles of lines A and B

FIGURE 50: A) STM of a (4×4) reconstructed surface. The line profiles in B) show the periodicity close to four times the lattice constant of SrTiO_3 .

Annealing the (2×2) structure in UHV directly after depositing 1.5 \AA of strontium formed a new structure. LEED of this surface only shows a (2×2) symmetry but an STM analysis (see figure 50) showed that the reconstructed sites run along the $[100]$ and the $[010]$ directions with a periodicity of 1.42 nm and 1.54 nm , respectively. This is close to four times the unit cell of STO. Therefore this structure is assumed to be a (4×4) reconstruction, but we did not pursue this issue with much detail.

The two surfaces with (2×2) and $c(4 \times 2)$ reconstruction have also been investigated in terms of atomic and chemical composition. XPS and ISS have been applied to both reconstructed surfaces, and the resulting spectra are shown in figures 51 and 52. The XPS spectrum of the $c(4 \times 2)$ surface was shifted for better comparison. To be able to compare two different spectra, the intensity of the spectra has been divided by the photo-electron current, i.e., the drain current from the ground to the sample while acquiring a spectrum. The relative change in the chemical composition was determined by calculating the ratio of the intensity of a strontium and a titanium peak. For XPS, the ratio of the $\text{Sr } 3d_{5/2}$ and the $\text{Ti } 2p_{3/2}$ was taken. The intensity

of each peak was determined by fitting the peaks after subtracting a Shirley background. For ISS, the peak intensity was determined by integrating over the peak area after subtracting a linear background. The error of each spectrum was determined by assuming Poisson distributed measurement values and by using the propagation of uncertainty. Table 6 shows the ratio of the intensities of the XPS and the ISS spectra. Within the uncertainty of XPS and peak-fitting, the XPS signal does not show any difference in chemical composition. This is most likely due to the fact that the XPS spectra were taken with normal emission (analyzer normal to the sample surface). This allows the photoelectrons to originate from deeper layers. Therefore the spectrum is assumed to be governed by the signal of the bulk SrTiO_3 . The ratio in intensity of the ISS signal however shows a clear excess of strontium on the (2×2) reconstructed surface. ISS is considered being very surface sensitive since the probability of neutralization of the ions is very high especially when traveling through matter.

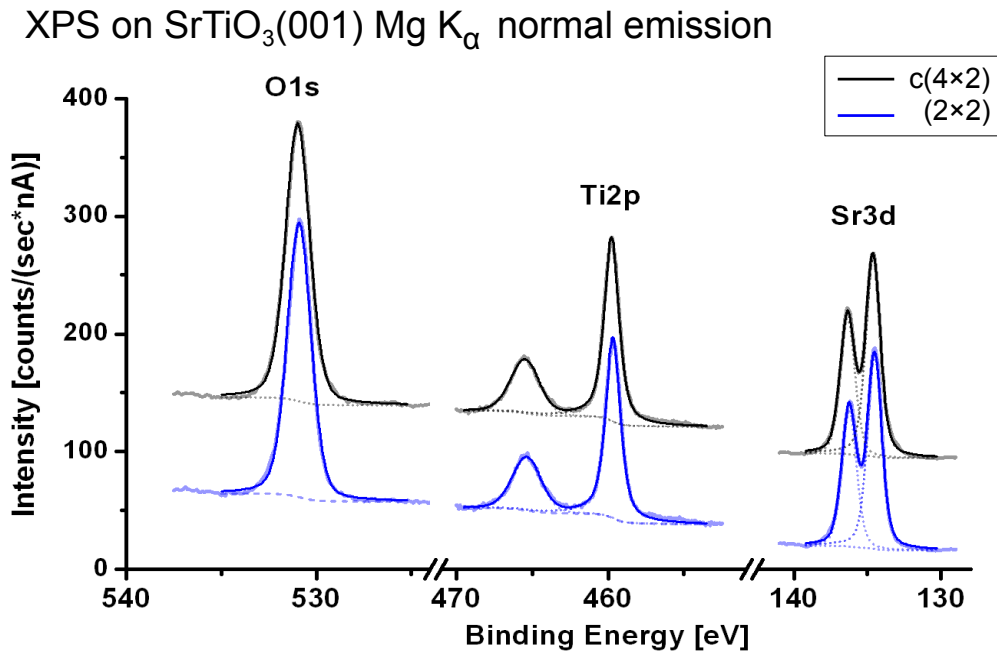


FIGURE 51: XPS spectra of both, a (2×2) and $c(4 \times 2)$ reconstructed $\text{SrTiO}_3(001)$ surface: The intensity of the $\text{Sr } 3d_{5/2}$ and of the $\text{Ti } 2p_{3/2}$ is compared for both spectra. The spectrum of the $c(4 \times 2)$ surface was shifted for comparison.

ISS on SrTiO₃(001) He⁺ 1keV 137°

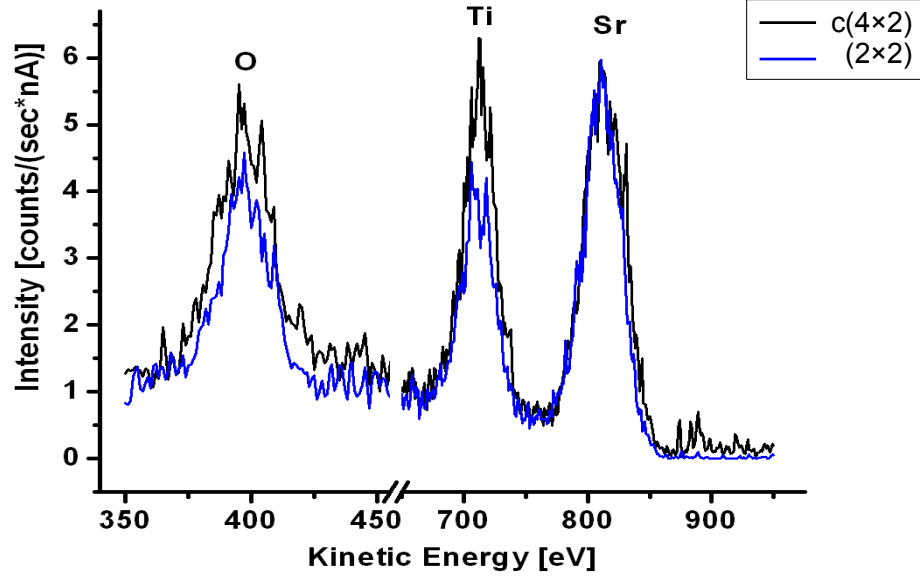


FIGURE 52: ISS spectra of both, a (2×2) and c(4×2) reconstructed SrTiO₃(001) surface: The intensity of the Sr and the Ti peak was compared for both spectra.

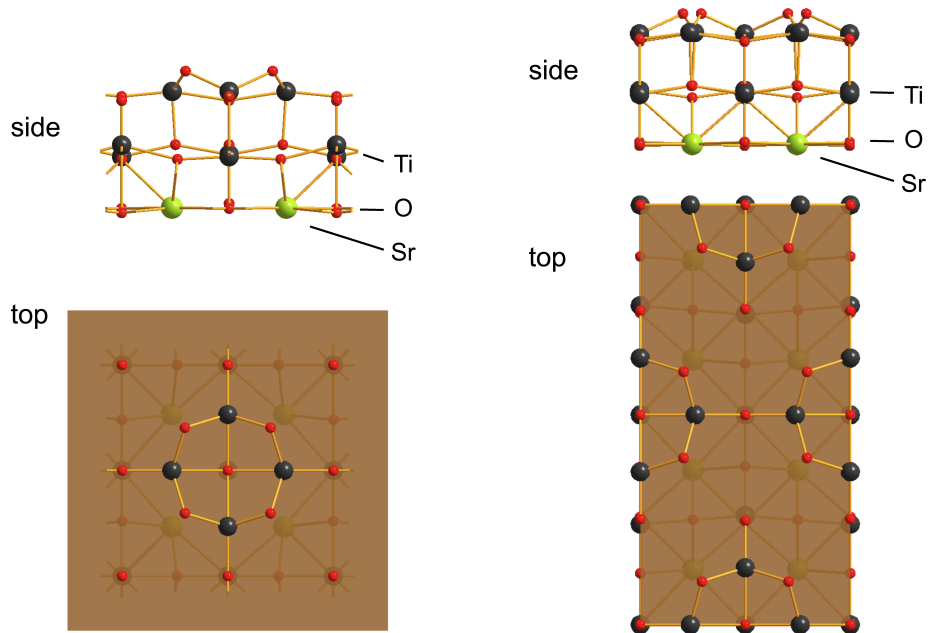
XPS	(2×2)	c(4×2)
Intensity $\frac{\text{Sr } 3d_{5/2}}{\text{Ti } 2p_{3/2}}$	1.03 ± 0.02	1.06 ± 0.02

ISS	(2×2)	c(4×2)
Intensity $\frac{\text{Sr}}{\text{Ti}}$	1.92 ± 0.14	1.40 ± 0.13

TABLE 6: Top: The ratio of the intensity of the Sr 3d_{5/2} and the Ti 2p_{3/2} peaks after peak fitting. Bottom: The ratio of the integrated intensity of the Sr and the Ti peak in ISS taking into account a linear background. The errors have been determined by Poisson statistical propagation of uncertainty.

5.2 Discussion of Experiments and Structure Models Proposed in the Literature

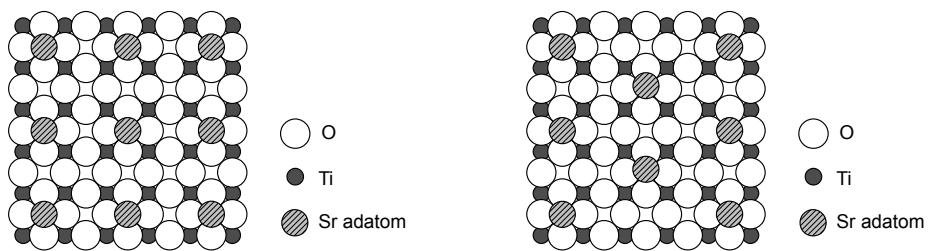
The results of the deposition experiments indicate a different surface stoichiometry for the $c(4\times 2)$ and the (2×2) reconstructions. Furthermore the different appearance of the step edges, seen in STM, indicates a different structure for both reconstructions. This assumption is also supported by the result of the ISS experiments, which showed an excess of strontium on the (2×2) reconstructed surface. These results are in contradiction to models proposed in the literature. Laurence Marks and coworkers proposed models for the $c(4\times 2)$ [61] and the (2×2) [62] reconstructions employing a TiO_2 overlayer on top of the TiO_2 terminated bulk $\text{SrTiO}_3(001)$. Figure 53 shows the crystal models developed by Marks' group. The contradiction lies in the identical stoichiometry of the surface layer of these models. Kubo and Nozoye proposed a different model [25]. They claim that the reconstruction stems from ordered strontium adatoms on a TiO_2 terminated $\text{SrTiO}_3(001)$ surface. Also this model is in contradiction with our results, because the coverage of reconstructed Sr adatoms on both structures, $c(4\times 2)$ and (2×2) , is equal $\theta=0.25$. Therefore also this model exhibits an equal surface stoichiometry for both structures. Figure 54 shows the structure models proposed by Kubo and Nozoye. The proposed models for the $c(4\times 2)$ and the (2×2) reconstructions are inherently similar. The difference is only that for the $c(4\times 2)$, every second row of reconstructed sites is shifted by one unit cell but the overall amount of reconstructed sites is equal. This makes every model, which employs the same reconstructed species for both structures, inconsistent with our experiments. Another indication of a different building block for the surface reconstructions is the appearance of the step edges. While the $c(4\times 2)$ reconstructed surface shows straight step edges along the $[001]$ and $[010]$ direction, the (2×2) structure shows wavy step edges. It is impossible to explain this difference by a model where every second row of the surface building blocks is shifted by one unit cell.



A) (2×2) structure model

B) $c(4 \times 2)$ structure model

FIGURE 53: Proposed structure models for the (2×2) and $c(4 \times 2)$ surface reconstructions of the $\text{SrTiO}_3(001)$ surface. Both models exhibit a surface layer stoichiometry of TiO_2 . Images taken from references [61] and [62].



A) (2×2) structure model

B) $c(4 \times 2)$ structure model

FIGURE 54: Proposed structure models for the (2×2) and $c(4 \times 2)$ surface reconstructions of the $\text{SrTiO}_3(001)$ surface. Both models exhibit a Sr-adatom coverage of $\theta = 0.25$. Images adapted from reference [25].

6 Summary and Conclusions

We studied the (4×1) reconstructed $\text{SrTiO}_3(110)$ surface with x-ray absorption spectroscopy (XAS) at the synchrotron facility MAXLab in Lund, Sweden. We performed XAS in two modes, i.e., bulk and surface sensitive mode, described in section 3.3. In the surface sensitive XAS spectrum an additional peak arises, which is a signature of titanium atoms in tetrahedral coordination in the surface region (see figures 35 and 36). This is in perfect agreement with the structure model proposed by Enterkin et al. [56]. In their model, the (4×1) structure is proposed as part of a homologous series of $(n\times 1)$ ($n = 6, 5, 4$) reconstructions. This series is also part of a surface phase diagram proposed by Wang et al. [34]. Since Wang et al. showed that the members of the $(n\times 1)$ series can be changed into each other reversibly by controlling the surface stoichiometry, i.e., by depositing titanium or strontium followed by annealing in oxygen, the confirmation of the tetrahedral coordination of the (4×1) structure also supports the other structure models of the $(n\times 1)$ series.

We used low-energy (45 eV) synchrotron radiation to probe the valence band region of the sample. Specifically, we studied the band gap region, i.e., the region of binding energies from the Fermi level (binding energy of zero) to binding energies of around 3 eV. An as-prepared (4×1) reconstructed $\text{SrTiO}_3(110)$ sample shows UPS spectra with a prominent valence band, which originates mainly from oxygen 2p states, and a flat band gap with a width of around 3 eV (see figure 25). We found that prolonged exposure to synchrotron light, e.g., during acquisition of XAS spectra, produces a significant state (peak) inside the band gap region. By dosing oxygen gas in situ, we found that this state vanishes. The in-gap state can therefore be related to the formation of oxygen vacancies. The process of the creation of oxygen vacancies upon incident radiation has already been discussed by Knotek and Feibelman [59]. The study of defect induced in-gap states is of great interest since it was found that the in-gap states support surface reactions, i.e., photocatalysis and photolysis [7].

Santander-Syro et al. found that cleaved $\text{SrTiO}_3(001)$ surfaces show the creation of two dimensional electron gases (2DEG) [10]. They concluded that the creation of oxygen vacancies during the cleaving process provides the electrons forming the 2DEG. Since oxygen vacancies are chemically very reactive and also represent a lattice defect, it is probably not the best way for doping the surface. STM images of a (4×1) reconstructed $\text{SrTiO}_3(110)$ surface show that single strontium adatoms exist on top of the reconstruction rows (see figure 27). Since strontium shows the $[\text{Kr}] 5s^2$ electron configuration, it is assumed that strontium is able to dope the surface with two

electrons. The fact that it adsorbs on the surface and therefore does not introduce a lattice defect makes it a promising surface dopant. Therefore we studied the thermal stability of Sr adatoms on the (4×1) reconstructed $\text{SrTiO}_3(110)$ surface. By depositing strontium, we increased the density from an as-prepared density of 0.12 Sr adatoms per nm^2 up to 0.16 Sr adatoms per nm^2 and further to 0.19 Sr adatoms per nm^2 . Annealing to $\sim 340^\circ\text{C}$ in 10^{-6} mbar O_2 was applied after each deposition to assure reordering and the density has been evaluated by STM image processing. The graph comparing the deposition and the resulting Sr adatom density (figure 32a) shows that we did not reach the saturation coverage and did not loose Sr adatoms during the soft annealing. Increasing the temperature systematically shows that Sr adatoms with a density of around 0.16 adatoms per nm^2 are stable on the (4×1) surface up to temperatures of about 650°C . Sr adatoms are therefore assumed to be relatively stable and further research of this topic is already ongoing, i.e., we recently performed ARPES measurements on the Sr adatom-doped $\text{SrTiO}_3(110)$ (4×1) reconstructed surface. A clear and prominent metallic state was found. This state also showed the energy dispersion and quantization of a 2DEG. This is very promising and will be pursued in the future.

One topic of this thesis was to find out if $\text{SrTiO}_3(001)$ surface reconstructions can also be interchanged like Wang et al. reported for the (110) surface. By sputtering and annealing we were able to prepare an atomically flat surface with terraces of one unit cell of STO step height showing a two-domain $c(4\times 2)$ symmetry in LEED. We deposited strontium metal onto this surface and annealed it in 10^{-6} mbar O_2 . The surface structure changed into a (2×2) structure, again determined with LEED. The amount of Sr deposited to change the structures was measured with a QCM to be 3 \AA . A reversible transition could be obtained by depositing titanium onto the (2×2) reconstructed surface. The amount of Ti deposited was measured to be around 0.35 \AA . The factor of ten, between the amount of Sr and Ti deposited to change from one to another structure, can be translated to a factor of two, when taking into account the different density and atomic weight of Sr and Ti. Additional deposition of Sr (2 \AA) onto a (2×2) reconstructed surface changes the surface to show a (1×1) symmetry in LEED. Again deposition of Ti (0.4 \AA) drives the structure back to the (2×2) structure. In addition we found that sputtering the sample drives the reconstructions towards the $c(4\times 2)$ structure and further to a structure called "waffle"-structure (named by Marks and coworkers [63]). Although simple sputter theory predicts that, in addition to oxygen, titanium should be preferentially sputtered away (because of the better mass-match with Ar^+), sputtering and annealing in oxygen seems to act titanium enriching.

An STM study of the two surface reconstructions showed that, prior to and after deposition and annealing in oxygen, we are able to obtain atomically flat terraces with one unit cell of STO step height. The different appearance of the step edges of the (2×2) and the $c(4\times 2)$ structures indicates that the two structures exhibit a different building block. The $c(4\times 2)$ reconstruction could be imaged with STM in atomic resolution, showing both domains coexist on the surface. The (2×2) reconstructed surface could not be scanned with high resolution in STM. A possible reason for this could be a low conductivity of the surface layer. Therefore these surfaces have been flashed to high temperatures in UHV for around 5 min. The resulting surface could be scanned with atomic resolution. The STM images revealed a $c(4\times 4)$ structure, there were also weak $c(4\times 4)$ spots in the LEED images. Another structure that formed upon flashing the sample to high temperatures in UHV was revealed in high resolution STM images. It showed a periodicity along $[100]$ and $[010]$ directions of close to four times the unit cell of STO. Although LEED does only show a (2×2) pattern, this structure is assumed to exhibit a (4×4) symmetry. The difference in preparation, to the obtained $c(4\times 4)$, could have been the flashing of the sample in UHV directly after Sr deposition, but this issue was not pursued with much detail.

Since the preparation procedures indicate a different surface chemical composition, we performed XPS and ISS on a (2×2) and a $c(4\times 2)$ reconstructed surface. By calculating the ratio of the characteristic peaks of Sr3d and Ti2p after peak fitting, we are able to compare the relative composition of strontium to titanium for each reconstruction. We found that with XPS in normal emission (see figure 51) we do not see any difference. Probably this is because XPS in normal emission shows information of the first few atomic layers. However, applying ISS reveals a different composition. This is because ISS only probes the first atomic layer. When calculating the ratio of the strontium to the titanium peak after subtracting a linear background in the ISS spectra (see figure 52), we see that the (2×2) structure is rich in strontium and therefore the $c(4\times 2)$ is more rich in titanium. This corresponds to the preparation procedure and also indicates that the two structures exhibit a different surface stoichiometry.

These results are in contradiction to models of the (2×2) and the $c(4\times 2)$ structure proposed in the literature. Two models were discussed. One model was proposed by Marks et al. [61, 62] and consists of a TiO_2 structure on top of a TiO_2 bulk terminated $\text{SrTiO}_3(001)$ plane. The proposed building block for both structures is equal and it therefore shows an equal surface stoichiometry. Another model proposed by Kubo and Nozoye [25] consists of ordered strontium adatoms building the reconstructions. Since the (2×2) and the $c(4\times 2)$ structure are inherently similar (the only difference is a shift

by one unit cell of STO in every second row of reconstructed sites), also this structure model exhibits an equal stoichiometry per surface unit area. This makes every model using an equal building block for both reconstructions to be in contradiction with our results.

Marks et al. proposes titanium with a pentahedral coordination in the (2×2) and the $c(4 \times 2)$ structure models. Therefore XAS could also be applied to test this prediction.

Capacitances between STM Scanner pins (Plug C)			
	Specifications report [nF]	12/06/2012 [nF]	12/10/2012 [nF]
PinA-PinC center-(y-)	0.28	0.261	0.320
PinA-PinD center-(x+)	0.27	0.205	0.314
PinA-PinE center-(y+)	0.32	0.258	0.332
PinA-PinF center-(x-)	0.29	0.279	0.333

TABLE 7: Capacitances measured between pins on plug C (STM scanner). The capacitances have been measured using an LCR bridge meter. One measurement (highlighted in red) showed a significantly lower capacitance (12/06/2012). This is assumed to have caused the distortion in the STM images. After repolarization (on 12/10/2012), the values are in the same range for each scanning direction.

Appendix A STM Scanner Repolarization

In the first half of this work, the scanner of the STM had problems. The resulting images were heavily skewed and the images had to be undistorted during image processing with ImageJ. Figures 28, 30, 31, 33, 38, 42a and 49a are examples of STM images that had to be undistorted. The reason was found to be related to the polarization of the STM scanner tube. By measuring the capacitances between the central electrode and the other electrodes (two for each scanning direction) of the STM scanner, we found that the capacitance between z-electrode (in the center of the scanner) and x+ is significantly smaller than the capacitances of the other three directions (see table 7). Figure 55 shows a schematic of the STM scanner and the assignment of the pins of the STM plugs. SPECS GmbH provided a solution for this problem. The scanner tube can be repolarized by applying an appropriate voltage (900 V, max $\frac{100V}{min}$, 1 hour) between the electrodes of the scanner tube. If this does not work properly, the same procedure should be carried out while heating the STM scanner to higher temperatures (100°C).

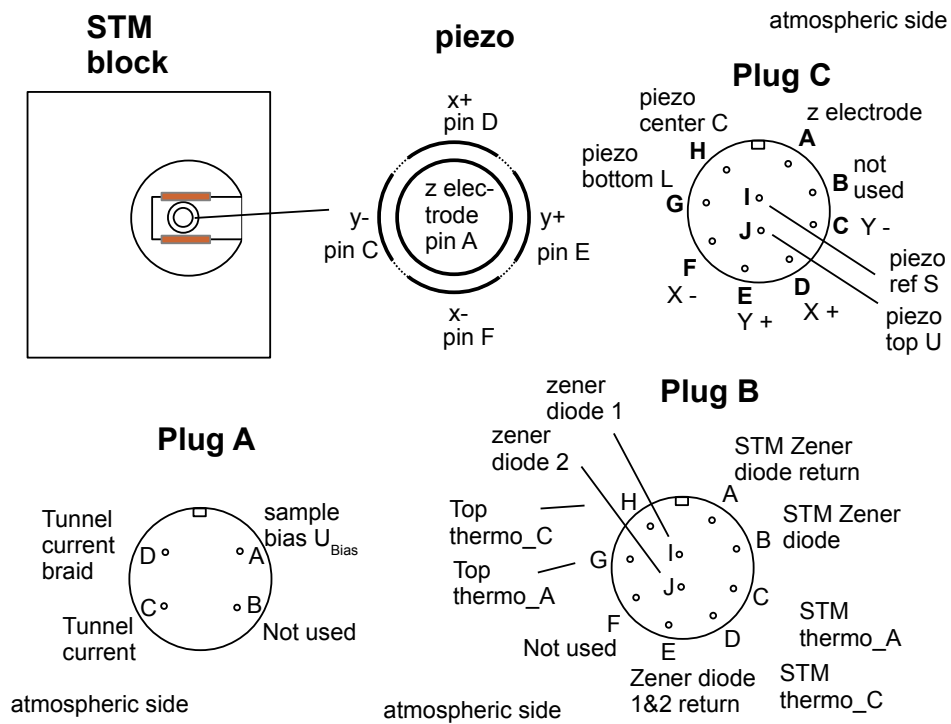


FIGURE 55: Pin assignment of the STM plugs. Plug C is driving the STM scanner, plug B is for heating the STM, and plug A is for the tunneling current and the sample bias. Capacitances have been measured at plug C between pin A and pin C, D, E and F, respectively. These pins are connected to the electrodes (center, x+, x-, y+, and y-) of the STM scanner tube.

References

- [1] P. Cox, *Transition Metal Oxides, An introduction to their electronic structure and properties*. Clarendon Press - Oxford, 1992.
- [2] A. Muñoz-Páez, “Transition Metal Oxides: Geometric and Electronic Structures,” *Journal of Chemical Education*, vol. 71, p. 381, 1994.
- [3] N. F. Mott, *Metal-Insulator Transitions*. Taylor & Francis, 1990.
- [4] J. Schooley and W. Hosler, “Superconductivity in Semiconducting SrTiO₃,” *Physical Review Letters*, vol. 12, no. 17, p. 474, 1964.
- [5] J. Bednorz and K. A. Mueller, “Perovskite-type Oxides - The New Approach to High-T_c Superconductivity,” *Nobel lecture*, 1987.
- [6] A. Fujishima and K. Honda, “Electrochemical Photolysis of Water at a Semiconductor Electrode,” *Nature*, vol. 238, p. 37, 1972.
- [7] J. Yin, J. Ye, and Z. Zou, “Enhanced photoelectrolysis of water with photoanode Nb:SrTiO₃,” *Applied Physics Letters*, vol. 85, no. 4, p. 689, 2004.
- [8] G. Korotcenkov, “Metal oxides for solid-state gas sensors: What determines our choice?,” *Materials Science & Engineering B*, vol. 139, pp. 1–23, 2007.
- [9] R. Sum, H. Lang, and H.-J. Guentherodt, “Scanning force microscopy study of single-crystal substrates used for thin-film growth of high-temperature superconductors,” *Physica C*, vol. 242, pp. 174–182, 1995.
- [10] A. Santander-Syro *et al.*, “Two-dimensional electron gas with universal subbands at the surface of SrTiO₃,” *Nature*, vol. 469, p. 189, 2011.
- [11] A. Ohtomo and H. Hwang, “A high-mobility electron gas at the LaAlO₃/STO₃ heterointerface,” *Nature*, vol. 427, p. 423, 2004.
- [12] D. G. Schlom and J. Mannhart, “Interface takes charge over Si,” *Nature Materials*, vol. 10, p. 168, 2011.
- [13] G. Chiarotti *et al.*, *The Landolt-Boernstein Database: Chapter 1.6 Crystal structures and bulk lattice parameters of materials quoted in the volume*. Springer Materials, 1993.

- [14] V. E. Henrich, G. Dresselhaus, and H. Zeiger, "Surface defects and the electronic structure of SrTiO₃ surfaces," *Physical Review B*, vol. 17, p. 4908, 1978.
- [15] G. Koster, G. Rijnders, D. H. Blank, and H. Rogalla, "Surface morphology determined by (001) single-crystal SrTiO₃ termination," *Physica C*, vol. 339, pp. 215–230, 2000.
- [16] M. Kawasaki *et al.*, "Atomic Control of the SrTiO₃ Crystal Surface," *Science*, vol. 266, p. 1540, 1994.
- [17] J. E. Andersen and P. J. Møller, "Impurity-induced 900 °C (2×2) surface reconstruction of SrTiO₃(001)," *Applied Physics Letters*, vol. 56, p. 1874, 1990.
- [18] P. van der Heide, Q. Jiang, Y. Kim, and J. Rabalais, "X-ray photoelectron spectroscopic and ion scattering study of the SrTiO₃(001) surface," *Surface Science*, vol. 473, p. 59, 2001.
- [19] Q. Jiang and J. Zegenhagen, "SrTiO₃(001) surfaces and growth of ultrathin GdBa₂Cu₃O_{7-x} films studied by LEED/AES and UHV-STM," *Surface Science*, vol. 338, p. L882, 1995.
- [20] B. Cord and R. Courths, "Electronic study of SrTiO₃(001) surfaces by photoemission," *Surface Science*, vol. 162, p. 34, 1985.
- [21] M. R. Castell, "Nanostructures on the SrTiO₃(001) surface studied by STM," *Surface Science*, vol. 516, p. 33, 2002.
- [22] M. Naito and H. Sato, "Reflection high-energy electron diffraction study on the SrTiO₃ surface structure," *Physica C*, vol. 229, p. 1, 1994.
- [23] M. R. Castell, "Scanning tunneling microscopy of reconstructions on the SrTiO₃(001) surface," *Surface Science*, vol. 505, p. 1, 2002.
- [24] Soo-hyon Phark, Y. J. Chang, and T. W. Noh, "Selective growth of perovskite oxides on SrTiO₃ (001) by control of surface reconstructions," *Applied Physics Letters*, vol. 98, p. 161908, 2011.
- [25] T. Kubo and H. Nozoye, "Surface structures of SrTiO₃(100)," *Surface Science*, vol. 542, p. 177, 2003.
- [26] Q. Jiang and J. Zegenhagen, "c(6×2) and c(4×2) reconstruction of SrTiO₃ (001)," *Surface Science*, vol. 425, p. 343, 1999.

- [27] C. Lanier *et al.*, “Atomic-scale structure of the SrTiO₃ (001)- $c(6 \times 2)$ reconstruction: Experiments and first-principles calculations,” *Physical Review B*, vol. 76, p. 045421, 2007.
- [28] Q. Jiang and J. Zegenhagen, “SrTiO₃ (001)- $c(6 \times 2)$: a long-range, atomically ordered surface stable in oxygen and ambient air,” *Surface Science*, vol. 367, p. L42, 1996.
- [29] T. Kubo and H. Nozoye, “Surface Structure of SrTiO₃ (001)- $(\sqrt{5} \times \sqrt{5})$ -R26.6°,” *Physical Review Letters*, vol. 86, p. 1801, 2001.
- [30] I. Shiraki and K. Miki, “SrTiO₃(100) - $(\sqrt{5} \times \sqrt{5})$ R26.6° surface observed by high-resolution scanning tunneling microscopy,” *Surface Science*, vol. 605, pp. 1304–1307, 2011.
- [31] M. S. M. González *et al.*, “In situ reduction of (110) SrTiO₃,” *Solid State Sciences*, vol. 2, p. 519, 2000.
- [32] J. Brunen and J. Zegenhagen, “Investigation of the SrTiO₃ (110) surface by means of LEED, scanning tunneling microscopy and Auger spectroscopy,” *Surface Science*, vol. 389, p. 349, 1997.
- [33] H. Bando *et al.*, “Structure and electronic states on reduced SrTiO₃(110) surface observed by scanning tunneling microscopy and spectroscopy,” *Journal of Vacuum Science and Technology B*, vol. 13, p. 1150, 1995.
- [34] Z. Wang *et al.*, “Evolution of the surface structures on SrTiO₃(110) tuned by Ti or Sr concentration,” *Physical Review B*, vol. 83, p. 155453, 2011.
- [35] Y. Haruyama *et al.*, “Annealing temperature dependence of the electronic structure of the reduced SrTiO₃ (111) surface,” *Journal of Electron Spectroscopy and Related Phenomena*, vol. 88-91, p. 695, 1998.
- [36] B. C. Russel and M. R. Castell, “ $(\sqrt{13} \times \sqrt{13})$ R13.9° and $(\sqrt{7} \times \sqrt{7})$ R19.1° reconstructions of the polar SrTiO₃ (111) surface,” *Physical Review B*, vol. 75, p. 155433, 2007.
- [37] B. C. Russel and M. R. Castell, “Surface of Sputtered and Annealed Polar SrTiO₃(111): TiO_x-Rich $(n \times n)$ Reconstructions,” *J. Phys. Chem. C*, vol. 112, p. 6538, 2008.
- [38] M. Schmid, “Experimentelle Methoden der Oberflächenphysik,” Lecture Notes, Vienna University of Technology, 2011.

- [39] C. Davisson and L. Germer, “Diffraction of Electrons by a Crystal of Nickel,” *The Physical Review*, vol. 30, no. 6, p. 705, 1927.
- [40] C. Brundle, “Elucidation of Surface Structure and Bonding by Photoelectron Spectroscopy,” *Surface Science*, vol. 48, pp. 99–136, 1975.
- [41] H. Ibach and H. Lüth, *Festkörperphysik*. Springer, 2008.
- [42] K. Hermann and M. Van Hove, “LEEDpat version 3.0.” <http://www.fhi-berlin.mpg.de/KHsoftware/LEEDpat/index.html>, 2010.
- [43] A. Einstein, “Über einen die Erzeugung und Verwandlung des Lichtes betreffenden heuristischen Gesichtspunkt,” *Annalen der Physik*, vol. 322, pp. 132–148, 1905.
- [44] W. Werner, “Tutorial on Quantitative Surface Analysis by means of Electron Spectroscopy,” Figure in online Tutorial (http://eaps4.iap.tuwien.ac.at/~werner/qes_tut_exp.html).
- [45] F. Kling, “Quantum Tunneling,” Figure in Wikipedia entry (http://en.wikipedia.org/wiki/Quantum_tunnelling).
- [46] G. Binnig *et al.*, “Surface Studies by Scanning Tunneling Microscopy,” *Physical Review Letters*, vol. 49, p. 57, 1982.
- [47] C. J. Chen, *Introduction to Scanning Tunneling Microscopy*. Department of Applied Physics and Applied Mathematics, Columbia University, New York: Oxford University Press, second edition ed., 2008.
- [48] W. Rasband, “ImageJ,” U.S. National Institutes of Health, Bethesda, Maryland, USA, (<http://imagej.nih.gov/ij/>), 1997–2012.
- [49] K. Singh and B. A. Kumar, “Electronics and Software for Scanning Tunneling Microscope,” A pdf document on STM Electronics (<http://www.iuac.res.in/~elab/phoenix/STM/stme.pdf>).
- [50] M. Schmid, “The Surface Structure, Deposition & Adsorption Calculator,” Website of the IAP, TU Wien (<http://www.iap.tuwien.ac.at/www/surface/surfcryst>), 2002–2012.
- [51] R. Nyholm *et al.*, “Beamline I311 at MAX-LAB: a VUV/soft X-ray undulator beamline for high resolution electron spectroscopy,” *Nuclear Instruments and Methods in Physics Research A*, vol. 467–468, pp. 520–524, 2001.

- [52] A. Damascelli, Z. Hussain, and Z.-X. Shen, “Angle-resolved photoemission studies of the cuprate superconductors,” *Reviews of Modern Physics*, vol. 75, p. 473, 2003.
- [53] J. Uhlig, “X-ray absorption spectroscopy,” Online Tutorial (<http://www.chemphys.lu.se/research/techniques/xrayxas/>).
- [54] I. Arcon, “Extended x-ray absorption fine structure,” Online Tutorial (<http://www.ung.si/~arcon/xas/exafs/exafs.htm>).
- [55] C. Noguera, “Polar Oxide Surfaces,” *J. Phys.: Condens. Mater*, vol. 12, pp. R367–R410, 2000.
- [56] J. A. Enterkin *et al.*, “A homologous series of structures on the surface of SrTiO₃(110),” *Nature Materials*, vol. 9, p. 254, 2010.
- [57] F. Li *et al.*, “Reversible Transition between Thermodynamically Stable Phases with Low Density of Oxygen Vacancies on the SrTiO₃(110) Surface,” *Physical Review Letters*, vol. 107, p. 036103, 2011.
- [58] Y. Aiura *et al.*, “Photoemission study of the metallic state of lightly electron-doped SrTiO₃,” *Surface Science*, vol. 515, pp. 61–74, 2002.
- [59] M. Knotek and P. J. Feibelman, “Ion Desorption by Core-Hole Auger Decay,” *Physical Review Letters*, vol. 40, p. 964, 1978.
- [60] E. Stavitski and F. de Groot, “The CTM4XAS program for EELS and XAS spectral shape analysis of transition metal L edges,” *Micron*, vol. 41, pp. 687–694, 2010.
- [61] N. Erdman *et al.*, “Surface Structures of SrTiO₃ (001): A TiO₂-rich Reconstruction with a c(4×2) Unit Cell,” *J. Amer. Chem. Soc.*, vol. 125, p. 10050, 2003.
- [62] Y. Lin *et al.*, “The (2×2) reconstructions on the SrTiO₃(001) surface: A combined scanning tunneling microscopy and density functional theory study,” *Surface Science Letters*, vol. 605, pp. L51–L55, 2011.
- [63] D. S. Deak *et al.*, “Ordering of TiO₂-Based Nanostructures on SrTiO₃ (001) Surfaces,” *J. Phys. Chem. B*, vol. 110, pp. 9246–9251, 2006.